Journal of Controlled Release 316 (2019) 331–348

Contents lists available at ScienceDirect

Journal of Controlled Release

journal homepage: www.elsevier.com/locate/jconrel

Porous poly(ε-caprolactone) implants: A novel strategy for efficient intraocular drug delivery

Raquel Boia[a,b,c,1], Paulo A.N. Dias[d,1], Joana M. Martins[a,b,c], Caridad Galindo-Romero[e,f], Inês D. Aires[a,b,c], Manuel Vidal-Sanz[e,f], Marta Agudo-Barriuso[e,f], Hermínio C. de Sousa[d,**], António Francisco Ambrósio[a,b,c], Mara E.M. Braga[d,**], Ana Raquel Santiago[a,b,c,*]

[a] Coimbra Institute for Clinical and Biomedical Research (iCBR), Faculty of Medicine, University of Coimbra, 3000-548 Coimbra, Portugal
[b] CNC, IBILI Consortium, University of Coimbra, Portugal
[c] Center for Innovative Biomedicine and Biotechnology (CIBB), University of Coimbra, Portugal
[d] CIEPQPF, Department of Chemical Engineering, University of Coimbra, Coimbra, Portugal
[e] Departamento de Oftalmología, Facultad de Medicina, Universidad de Murcia, Murcia, Spain
[f] Instituto Murciano de Investigación Biosanitaria Hospital Virgen de la Arrixaca (IMIB-Virgen de la Arrixaca), Spain

ARTICLE INFO

Keywords:
Poly (ε-caprolactone)
Biodegradable porous implants
Supercritical carbon dioxide foaming/mixing method
Intraocular drug delivery
Safety
Retina

ABSTRACT

This work reports the development of porous poly (ε-caprolactone) (PCL)-based intraocular implants, prepared by green supercritical carbon dioxide ($scCO_2$) foaming/mixing method (SFM), to produce implants that degrade faster than typical slow-degrading PCL-based implants. The higher porosities and surface areas of these implants led to faster degradation rates at *in vitro* accelerated alkaline conditions than low porosity/surface area implants prepared by hot melting processing. These porous implants also presented distinct (faster) release rates of a test-drug (dexamethasone). Additionally, these porous devices did not cause cell death and did not reduce the number of neurons, indicating that are not toxic to retinal cells. We further explored the impact of PCL-based implant to the retina by *in vivo* evaluation and histological analysis. Implants were surgically inserted in the vitreous of Wistar rats, and their presence did not change the function, structure and anatomy of the retina. These devices demonstrated a good intraocular tolerance, further confirming their viability for prolonged drug delivery applications. Further comprehensive studies based on this promising preliminary assessment and proof-of-concept could enable its future translation to clinical protective strategies for retinal diseases.

1. Introduction

Chronic retinal diseases, as age-related macular degeneration (AMD), glaucoma and diabetic retinopathy, represent 84 % of visual impairment worldwide [1]. The therapeutic options mainly include topical drug administration using eye drops or intravitreal injections [1]. Topical drug delivery is non-invasive and easily performed by the patient [2], however the application of eye drops needs to be quite frequent and leads to poor patient compliance [3–6]. Intravitreal injections are currently the main method to deliver drugs into the posterior segment of the eye [7], however the need to maintain therapeutic drug levels require frequent injections that may cause several side effects such as inflammation, endophthalmitis, retinal detachment and cataracts [8]. Therefore, intraocular drug delivery systems based on biodegradable and biocompatible polymeric materials may have the potential to circumvent some of the aforementioned drawbacks [9–11]. These systems can be designed to maintain the therapeutic concentrations for extended periods, reducing the frequency of administration and increasing patient compliance [11]. The use of biodegradable polymeric drug delivery systems usually overcomes the need of surgical removal after the drug has been exhausted that happens in the case of non-biodegradable implants [11,12].

Poly(ε-caprolactone) (PCL) is a biocompatible and bioresorbable synthetic polymer approved by US Food and Drug Administration (FDA) that has been extensively studied and applied in implants for ophthalmic controlled drug delivery [10,13–15]. In particular, PCL

* Corresponding author at: Coimbra Institute for Clinical and Biomedical Research (iCBR), Faculty of Medicine, University of Coimbra, 3000-548 Coimbra, Portugal.
** Corresponding authors.
E-mail addresses: hsousa@eq.uc.pt (H.C. de Sousa), marabraga@eq.uc.pt (M.E.M. Braga), asantiago@fmed.uc.pt (A.R. Santiago).
[1] These authors contributed equally to this work.

https://doi.org/10.1016/j.jconrel.2019.09.023
Received 11 June 2019; Received in revised form 26 September 2019; Accepted 29 September 2019
Available online 09 November 2019

intraocular implants have been prepared for the delivery of dexamethasone [10,15]. In addition to the controlled delivery of drugs loaded within the matrix, which is mainly controlled by water sorption and by its hydrolytic degradation, PCL presents other important advantages such as its tailorable physical and mechanical properties, and ease of shaping and processing at relatively low temperatures [11,16].

Typical manufacturing techniques used to prepare these polymeric implants are hot melt-pressing (HM), extrusion, 3D-printing, injection moulding or solution casting [9]. However, these methods may involve hazardous solvents and/or operate at processing conditions (*e.g.*, temperature, pH) that could promote the degradation of the polymers, drugs and other additives [9,17]. Alternatively, the supercritical carbon dioxide ($scCO_2$)-assisted foaming/mixing (SFM) method can be used to avoid most of these problems. The temporary plasticizing effect of $scCO_2$ leads to operating temperatures considerably lower than typical polymer melting temperatures at atmospheric pressure, thus allowing sensitive drugs to be loaded at mild conditions. In addition, hazardous solvents are usually absent in this method. SFM methodologies have been successfully applied to several thermoplastic polymers, including PCL and other poly(α-esters), to obtain materials with tuneable physical and morphological properties, such as polymer crystallinity, porosity, pore size distributions, pore interconnectivity, and surface area, just by controlling the final depressurization step rate and/or the amount of absorbed CO_2 (and varying the other operational conditions such as processing time, temperature and pressure) [17–21]. The typical high porosities introduced in thermoplastic polymers by the SFM process may have the potential to increase the hydrolytic and enzymatic degradation rates of poly(α-esters), namely by increasing surface area, water sorption/swelling rates, and the available reaction sites at the surface, which are quite important advantageous features for slow degrading polymers such as PCL [22,23]. To the best of our knowledge, no porous implant (of the monolithic type) has yet reached the market. However, previous studies suggest that highly porous materials prepared by SFM can be designed for a better control of drug release [17].

Therefore, the present work aimed to use the SFM method to develop and to characterize a new, biodegradable and porous intraocular implant that may present faster degradation rates and, at the same time, still control the release of drugs over time. The morphologies, thermal properties and the degradation kinetics profiles (at accelerated alkaline conditions) of prepared SFM drug-free implants were assessed and compared with non-porous implants prepared by a typical HM process. Additionally, the safety of SFM drug-free implants to the retina was assessed by extended and meticulous *in vitro* and *in vivo* studies. Finally, these new implants were tested for the incorporation yields and for the *in vitro* release kinetics of a test-drug, dexamethasone, a well-known anti-inflammatory and immuno-suppressant glucocorticoid already used for the treatment of ocular pathologies [17,24–26].

2. Materials and methods

2.1. Implants processing

PCL pellets ($40\ k \leq M_n \leq 50\ kg\ mol^{-1}$, $48\ k \leq M_W \leq 90\ kg\ mol^{-1}$; Sigma-Aldrich, Missouri, USA) were processed into powder, as described previously [17], and mechanically sieved (sieve size 0.25 mm) to particle diameters smaller than 250 μm.

PCL, dexamethasone (DXMT, ≥98 %; Sigma-Aldrich) and glycofurol (G, 99 %, Sigma-Aldrich), mixtures (in different compositions, Table 1), were introduced into polyurethane micro-cylinder moulds (Optiva® I.V. 24 G catheters, Smiths Medical, Minnesota, USA), and processed by a supercritical carbon dioxide (≥99.998 %, v/v, Praxair, Portugal) foaming/mixing method, at fixed pressure (20 MPa), temperature (45 °C) and processing time (2 h) conditions. Three distinct depressurization rates (1–3 MPa min^{-1}) were employed. The employed experimental SFM set-up and the general followed procedures were previously described [17,18]. Additionally, and for comparison purposes, two other PCL-based mixtures (Table 1) were also processed by a two-step HM method: 30 min in an oven (at 1 atm, 50 °C), followed by an additional processing period of 30 min at 80 °C. The processed materials (cylindrical implants) were removed from the micro-cylindric moulds and cut to the desired dimensions (approximately 2 × 0.46 mm, length × diameter) under a stereo microscope (Leica, Wetzlar, Germany). Three batches/replicates (using 25–30 moulds/batch) were prepared for each tested process condition. Typically, 3–4 implants were obtained from each mould.

2.2. Morphological characterization

Drug-free implants prepared by SFM and HM were previously sputter-coated with a gold film or with gold/palladium mixture for 15 s (around 4 nm thickness), and analysed in scanning electron microscope (SEM) JSM-5310 (Jeol, Tokyo, Japan) or Vega3 (Tescan, Prague, Czech Republic), respectively, at 2 kV.

Processed implants obtained from three different batches (around 25–30 moulds/batch) were analysed (5 measurements) by helium picnometry (AccuPyc® 1330, Micromeritics Instrument Corp., Georgia, USA) to obtain the real densities, by nitrogen adsorption (ASAP 2000, Micromeritics Instrument Corp., Georgia, USA) to determine surface areas (Brunauer-Emmett-Teller, BET) and average pore diameters (Barrett-Joyner-Halenda, BJH), and by mercury intrusion porosimetry (Autopore IV 9500, Micromeritics Instrument Corp., Georgia, USA) to obtain pore size distribution, porosity, bulk density, and average pore diameter. A single set of implants was measured for each process condition; and, the process variability was taken into account by measuring implants prepared from the three different processing batches for each set.

2.3. Thermal properties

PCL powder (diameter < 250 μm) and drug-free implants prepared by SFM and HM were analysed by modulated differential scanning calorimetry (MDSC, Q100, TA Instruments, Delaware, USA). Calibration was made with Indium, and tests were performed for samples weighing ~5 mg, in aluminium pans and under a nitrogen atmosphere (50 $cm^3\ min^{-1}$), by starting at −80 °C for 5 min, modulating at ± 0.5 °C every 40 s, and heating up to 200 °C at 2 °C min^{-1}. Assessments were performed in duplicate to obtain the melting temperatures (T_m) and enthalpies ($\Delta H_f(T_m)$). The crystallinity degree ($\chi_c(\%)$) was determined by [27,28]:

$$\chi_c(\%) = \frac{\Delta H_f(T_m)}{\Delta H_f^0(T_f^0)} \times 100 \quad (1)$$

where $\Delta H_f^0(T_f^0)$ is the melting enthalpy of 100 % crystalline PCL, which is assumed to be 139.3 J g^{-1} [29].

2.4. Accelerated alkaline degradation tests

The *in vitro* hydrolysis degradation patterns of drug-free PCL-based implants formulated with glycofurol (PCL:DXMT:G, 92:00:08, wt.%) prepared by SFM and by HM were studied at accelerated alkaline conditions by adapting the method previously developed [29]. Samples of 1.3 mg (3 replicates for each tested processing method) were initially kept immersed overnight in bi-distilled water. Subsequently, samples were immersed in 3 mL of NaOH solution (5 M) (Sigma-Aldrich, Missouri, USA), in sealed glass tubes for 10 min; at room temperature, gently dried in filter paper and weighed to obtain the initial mass (m_0). The sealed tubes were kept in a thermoshaker, at 37 °C and 100 rpm, for sample degradation. Samples were removed and weighed (m_i) at several defined time intervals. The variation of mass ($\Delta m(\%)$) was determined by:

Table 1
Experimental design on the processing of PCL-based implants by SFM and HM: dexamethasone incorporation yields and correlated parameters obtained from the release kinetics diffusion and desorption models.

Method	Experimental design		Drug incorporation		Diffusion model		Desorption model		
	Depressurization rate (MPa min^{-1})	PCL:DXMT:G (wt.%)	DXMT/PCL (μg mg^{-1})	DXMT loaded (%)	D (cm^2 s^{-1}) × 10^{11}	RMSE	α	τ (days)	RMSE
SFM 20 MPa, 45 °C, 2 h	1	100:00:00	–	–	–	–	–	–	–
	2	100:00:00	–	–	–	–	–	–	–
	3	100:00:00	–	–	–	–	–	–	–
	2	92:00:08	–	–	–	–	–	–	–
		74:26:00	179.5 ± 12.4	51.1 ± 3.5	–	–	–	–	–
		66:26:08	389.7 ± 2.5	98.9 ± 0.6	7.15 ± 2.18	0.0618	0.65 ± 0.01	3.79 ± 0.30	0.0337
HM 50 °C, 0.5 h	–	92:00:08	–	–	–	–	–	–	–
followed by 80 °C, 0.5 h		66:26:08	388.5 ± 3.1	98.6 ± 0.8	3.02 ± 0.31	0.0294	0.58 ± 0.02	7.50 ± 1.03	0.0501

$$\Delta m(\%) = \frac{m_0 - m_i}{m_0} \times 100 \quad (2)$$

2.5. Animals

Adult Wistar rats were housed in a standard animal room under controlled environment with free access to food and water. All procedures were approved by the Animal Welfare Committee of the Coimbra Institute for Clinical and Biomedical Research of the Faculty of Medicine of University of Coimbra (ORBEA 23/2015) and were conducted in accordance to the Portuguese law (Decreto-Lei 113/2013) and to the Association for Research in Vision and Ophthalmology statement for animal use.

2.6. Safety for the retinal cells: in vitro experiments

2.6.1. Primary culture of rat retinal neural cells

Retinal neural cell cultures were obtained from 3-day-old Wistar rats, as previously described [30]. The cells were plated at a density of 2×10^6 cells cm^{-2} in 12-well plates with glass coverslips previously coated with poly-D-lysine (0.1 mg mL^{-1}; Sigma-Aldrich, Missouri, USA) and cultured in Eagle's minimum essential medium (Sigma-Aldrich, Missouri, USA), supplemented with 26 mM $NaHCO_3$, 25 mM HEPES, 10 % heat-inactivated fetal bovine serum (FBS; GIBCO, Invitrogen, Life Technologies, California, USA), penicillin (100 U mL^{-1}; Sigma-Aldrich, Missouri, USA), and streptomycin (100 g mL^{-1}; Sigma-Aldrich, Missouri, USA) in a humidified atmosphere of 5 % CO_2 at 37 °C for seven days. After one day in culture (one day *in vitro*, DIV1), cell cultures were incubated with PCL-based implants or with medium that was in contact with drug-free implants for 3 weeks (to check for the effects of any PCL degradation products).

2.6.2. Organotypic retinal cultures

The retinas from Wistar rats (8–10 weeks old) were dissected in Hanks' balanced salt solution (HBSS, in mM: 137 NaCl, 5.4 KCl, 0.45 KH_2PO_4, 0.34 Na_2HPO_4, 4 $NaHCO_3$, and 5 glucose; pH 7.4) and placed in tissue culture inserts with a 0.4 μm pore size (Millicell, Millipore, Massachusetts, USA), with the ganglion cell layer (GCL) facing up. The retinas were cultured for 4 days in Neurobasal-A medium (GIBCO, Invitrogen, Life Technologies, California, USA) supplemented with B27 (GIBCO, Invitrogen, Life Technologies, California, USA), 2 mM L-glutamine (Sigma-Aldrich, Missouri, USA) and gentamicin (50 mg mL^{-1}; GIBCO, Invitrogen, Life Technologies, California, USA), in 5 % CO_2 humidified atmosphere, as previously described [31].

The cultures were incubated with PCL-based implant for 24 h, 48 h and 72 h or with culture medium that was previously in contact for four weeks with these implants (PCL-based metabolites) for four days.

2.7. Safety for the retina: in vivo experiments

2.7.1. Surgical procedure for implantation of SFM-processed drug-free PCL-based implants

The animals were randomly assigned into sham-operated group or implant-inserted group. Animals were anesthetized with 2.5 % isoflurane (IsoFlo; Abbott Laboratories, Illinois, USA) with 1 L min^{-1} of O_2. Oxybuprocaine (4 mg mL^{-1}, Anestocil, Edol, Portugal) and tropicamide (10 mg mL^{-1}, Tropicil Top, Edol, Portugal) were applied topically for corneal anesthesia and mydriasis, respectively. One SFM-processed drug-free PCL-based implant (92:00:08, wt.%) was introduced in the vitreous with a 24-gauge catheter after making an incision in the sclera with a 23-gauge needle. Animals were sacrificed 4 and 8 weeks after the surgery.

2.7.2. Measurement of intraocular pressure (IOP)

Animals were trained for manipulation for IOP measurement during 2 weeks before surgical procedure. After implantation, IOP was measured bilaterally with a rebound tonometer specifically designed for rodents (Tonolab®, Icare, Finland), twice a week until sacrifice, as previously described [32]. An average of ten reliable measurements made in each eye was considered as one reading and reported as the IOP for that eye. The average of the IOP values obtained during the study interval was reported.

2.7.3. Optical coherence tomography (OCT)

Retinal structure was evaluated by OCT using a Micron IV (Phoenix Research Labs, California, USA) with a contact lens specifically designed for rat. The animals were anesthetized by intraperitoneal injection of ketamine (90 mg kg^{-1}; Nimatek, Dechra, UK) and xylazine (10 mg kg^{-1}; Sedaxylan, Dechra, UK). After topical anesthesia with oxybuprocaine (4 mg mL^{-1}, Anestocil, Edol, Portugal) and pupillary dilation with tropicamide (10 mg mL^{-1}, Tropicil Top, Edol, Portugal), both eyes were imaged and 13 B-scans centered in the optic nerve head were acquired. Total retinal thickness was obtained after segmentation using the semi-automatic segmentation software InSight (Phoenix Research Labs, California, USA).

2.7.4. Electroretinogram (ERG) recordings

Retinal activity was evaluated by electroretinography using corneal gold wire electrodes as previously described [33]. ERGs were performed under red dim light after overnight dark adaptation of the animals. Animals were anesthetized and topical anesthetic and mydriatic were applied, as described above. Methylcellulose (Methocel 2 %, OmniVision, California, USA) was applied for a good contact between cornea and gold ring electrode. A Ganzfeld stimulator (Roland Consult GmbH, Germany) with white light flashes (0.0095–9.49 cd-s m^{-2}) was used and scotopic ERG was recorded.

The amplitude (μV) and latency (ms) of a-wave and b-wave in

Table 2
List of primary and secondary antibodies used in this study.

	Supplier	Cat. No	Host	Dilution	Sample
Primary antibodies					
Anti-arrestin	Millipore	AB15282	Rabbit	1:500	Retinal cryosections
Anti-brn3a	Millipore	MAB1585	Mouse	1:200	Organotypic retinal cultures/Retinal cell cultures
	Santa Cruz Biotechnologies	sc-31984	Goat	1:750	Retinal whole-mounts
Anti-calbindin	Swant	CB-38a	Rabbit	1:500	Retinal cryosections
Anti-calnexin	Sicgen	AB0041-500	Goat	1:5000	Protein levels
Anti-GFAP	Millipore	IF03L	Mouse	1:500	Retinal cryosections/Protein levels
Anti-Iba1	Wako	019-19741	Rabbit	1:1000	Retinal cryosections
Anti-NeuN	Cell Signaling	D4G40	Rabbit	1:500	Retinal cell cultures
Anti-PKCα	Santa Cruz	sc-8393	Mouse	1:500	Retinal cryosections
Anti-rhodopsin	Millipore	MABN15	Mouse	1:500	Retinal cryosections
Anti-vimentin	Abcam	AB92547	Rabbit	1:500	Retinal cryosections
Secondary antibodies					
Alexa Fluor anti-rabbit 488	Life Technologies	A11008	Goat	1:500	
Alexa Fluor anti-mouse 568	Life Technologies	A11004	Goat	1:500	
Alexa Fluor anti-goat 594	Life Technologies	A11058	Donkey	1:500	
Alexa Fluor Anti-Rabbit 568	Life Technologies	A11036	Goat	1:200	
HRP-conjugate Anti-mouse	Bio-Rad	1706516	Goat	1:10000	
AP Anti-goat	Thermo Scientific	31300	Rabbit	1:10000	

scotopic conditions (reflecting rod response) were extracted. Off-line digital filter was applied on b-wave (high frequency cut-off of 50 Hz) with the RETIport software (Roland Consult GmbH, Germany).

2.8. Immunolabelling

2.8.1. Retinal cell cultures

Cell cultures were immunostained as previously described [34]. Cells were washed with phosphate-buffered saline (PBS, in mM: 137 NaCl, 2.7 KCl, 10 Na_2HPO_4, 1.8 KH_2PO_4; pH 7.4) and fixed with 4 % paraformaldehyde (PFA) with 4 % sucrose for 10 min. Then, cells were permeabilized with 1 % Triton X-100 and blocked with 3 % bovine serum albumin (BSA) and 0.2 % Tween 20. The cells were incubated with the primary antibody (Table 2), followed by incubation with the secondary antibodies (Table 2). The nuclei were stained by incubation with 4′,6-diamidino-2-phenylindole (DAPI; 1:2000; Invitrogen, Life Technologies, California, USA) for 10 min. The preparations were mounted with Glycergel mounting medium (DAKO, California, USA) and were observed in a fluorescence microscope (Axio Observer.Z1, Zeiss, Germany). For each condition, 10 images per coverslip were randomly acquired with a 20 × objective (Plan Achromat 20×/0.8 M27). In order to compare the different conditions, all images were acquired using identical gain and exposure settings.

2.8.2. Organotypic retinal cultures

Retinal organotypic cultures were immunostained as previously described [31]. Briefly, retinas were washed with PBS and fixed with ice-cold 100 % ethanol for 10 min at 4 °C. After washing with PBS, retinas were incubated with blocking solution (3 % BSA, 10 % normal goat serum and 0.1 % Triton X-100) for 1 h at room temperature. Samples were then incubated with the primary antibodies (Table 2) in blocking solution for 48 h at 4 °C, followed by incubation with the secondary antibodies (Table 2) overnight at 4 °C. Nuclei were counterstained with DAPI (1:1000; Invitrogen, Life Technologies, California, USA) and the samples were then flat-mounted on glass slides with the GCL facing upwards and cover slipped with Glycergel mounting medium (DAKO, California, USA).

The preparations were observed in a confocal microscope (Zeiss LSM 710, Germany) and images were randomly acquired with a 20× objective (Plan Achromat 20×/0.8 M27). From each retina, 3 images per quadrant were acquired (total of 12 images per sample). All images were acquired using identical gain and exposure settings to compare the different conditions.

2.8.3. Retinal cryosections

Retinal cryosections were prepared as previously described [32]. Retinal sections were permeabilized with 0.25 % Triton X-100 in PBS for 30 min and blocked in 10 % normal goat serum plus 1 % BSA in a humidified environment. Then, the sections were incubated with the primary antibodies (Table 2), followed by incubation with respective secondary antibodies (Table 2). Nuclei were counterstained with DAPI (1:2000; Invitrogen, Life Technologies, California, USA) and the slices were mounted with Glycergel mounting medium (DAKO, California, USA). The preparations were observed in a confocal microscope (Zeiss LSM 710, Germany) and images were acquired with a 20× objective (Plan Achromat 20×/0.8 M27).

2.8.4. Retinal whole-mounts

After transcardiac perfusion of animals, eyes were enucleated and retinas were dissected as flattened whole-mounts, as previously reported [35]. The retinas were permeabilized with 0.5 % Triton X-100 and incubated with the primary antibodies (Table 2). Retinas were incubated with the secondary antibodies (Table 2) and mounted with GCL side up and covered with anti-fading mounting medium.

Whole-mounted retinas were acquired with a 10× objective under an epifluorescence microscope (Axioskop 2 Plus; Zeiss Microscopy, Germany) equipped with a computer-driven motorized stage (ProScan H128 Series; Prior Scientific Instruments, UK), controlled by Image-Pro Plus (IPP 5.1 for Windows; Media Cybernetics, Maryland, USA), as previously described [35]. Reconstructed whole-mounts, made up from 154 individual frames, were further processed when required using Adobe Photoshop® CS 8.0.1 (Adobe Systems, Inc., California, USA).

The total population of $Brn3a^+$RGCs was automatically quantified by processing the individual Brn3a images taken for each retinal whole-mount with a specific cell-counted routine developed for the IPP software. Isodensity maps were generated with the IPP software to evaluate the spatial distribution of $Brn3a^+$RGCs throughout the entire retinal surface (for more details, see [35]).

2.9. Enzyme-linked immunosorbant assay (ELISA) for quantification of TNF and IL-1β protein levels

Protein levels of interleukin-1β (IL-1β) and tumor necrosis factor (TNF) were quantified in the culture medium supernatants and in the retinas by ELISA, according to the instructions provided by the manufacturer (PeproTech EC Ltd, UK) and as previously described [34].

2.10. Terminal deoxynucleotidyl transferase (TdT)-mediated dUTP nick end labeling (TUNEL) assay

Rat retinal neural cell cultures were fixed with 4 % PFA with 4 % sucrose for 10 min. Cell death was assessed using DeadEnd™ Fluorometric TUNEL System following the manufacturer's instructions (Promega, Wisconsin, USA). The nuclei were stained with DAPI (1:2000; Invitrogen, Life Technologies, California, USA). After washing, the preparations were mounted with Glycergel mounting medium (DAKO, California, USA). The preparations were observed in a fluorescence microscope (Axio Observer.Z1, Zeiss, Germany). For each condition, 10 images per coverslip were randomly acquired with a 20× objective (Plan Achromat 20×/0.8 M27).

2.11. Western blot

Retinas were lysed in ice-cold radioimmunoprecipitation assay (RIPA) buffer (50 mM Tris, 150 mM NaCl, 5 mM EGTA, 1 % Triton X-100, 0.5 % DOC, 0.1 % SDS) supplemented with 1 mM dithiothreitol (DTT, Sigma-Aldrich, Missouri, USA), complete miniprotease inhibitor cocktail tablets (Roche, Sigma-Aldrich, Missouri, USA) and phosphatase inhibitors (10 mM NaF and 1 mM Na_3VO_4) and protein extracts were prepared as previously described [36].

Samples (20 µg of protein) were separated in 8 % sodium dodecyl sulphate-poly(acrylamide) gel electrophoresis (SDS-PAGE) and the proteins were transferred electrophoretically to poly(vinylidene difluoride) (PVDF) membranes. The membranes were blocked in 5 % skim milk in Tris-buffered saline (TBS: 137 mM NaCl, 20 mM Tris-HCl, pH 7.6) containing 0.1 % Tween-20 (TBS-T) for 1 h at room temperature. The membranes were incubated with the primary antibodies (Table 2), followed by incubation with the corresponding secondary antibodies (Table 2). The membranes were processed for protein detection using ECL (Clarity™, Bio-Rad, California, USA) or ECF™ (GE Healthcare Amersham™, UK) in accordance with the manufacturer's instructions. Digital quantification of bands intensity was performed using ImageQuant 5.0 software (Molecular Dynamics, Inc., California, USA). Membranes were reprobed for calnexin as a loading control.

2.12. Drug incorporation yield and release kinetics

DXMT-loaded PCL implants prepared by SFM and HM from initial mixtures of PCL:DXMT:G (66:26:08, wt.%) were tested to determine the drug incorporation yields and the kinetics of drug release in water. Both tests were performed in triplicate and using samples of around 0.7 mg kept in sealed vials in a thermoshaker at 37 °C and 100 rpm. For the drug incorporation assessment, samples were kept in methanol (1.5 mL) and, every 2 h, aliquots (200 µL) were retrieved for analysis, and the solvent was replaced by fresh methanol. This procedure was repeated until a negligible amount of drug was detected (less than 0.5 % of the accumulated drug).

Kinetics of drug release experiments were performed in bi-distilled water (15 mL) under stirring (100 rpm) and aliquots (200 µL) were retrieved at defined time t intervals. The release profiles were obtained by plotting the percentage of released drug over time, which is given by:

$$\text{Released DXMT}\ (\%) = \frac{M_t}{M_0} \times 100 \tag{3}$$

where M_t is the amount of drug released at a given time, and M_0 is the mass of drug that was loaded into the implant. Results were correlated by applying well-known release kinetics models. The first model is based on the assumption that the drug is released from the polymer matrix simply by a diffusional process, after diffusion and absorption of water into the polymer. Assuming perfect sink conditions, the radial drug diffusion from a cylinder of radius r over time can be given by Refs. [37,38]:

$$\frac{M_t}{M_0} = 4\left(\frac{Dt}{\pi r^2}\right)^{1/2} - \frac{Dt}{r^2} \tag{4}$$

where D is the drug diffusivity within the polymer. The diffusion model presented by Eq. (4) is typically applied for less than 40 % of drug released.

The release of drug from slow degrading polymeric matrices such as PCL may not be dominated only by diffusion, and the desorption of the drug from the pores surface and from the outer implant surface are probably other additional controlling steps. This can be described by the following model [39,40]:

$$\frac{M_t}{M_0} = \alpha\left[1 - \exp\left(-\frac{\pi^2}{8}\frac{t}{\tau_r}\right)\right] \tag{5}$$

where τ_r is the specific process release time, and α is the porosity factor given by:

$$\alpha = \frac{M_{S0}}{M_{S0} + M_{b0}} < 1 \tag{6}$$

M_{S0} and M_{b0} are the fractions of the mass of drug loaded at the surface and at the bulk of the matrix, respectively, with $M_0 = M_{S0} + M_{b0}$.

Incorporated and released DXMT was quantified by high performance liquid chromatography (HPLC, Prominence UFLC, Shimadzu, Japan), coupled to a photo diode array detector (DAD, SPD-M20A, Shimadzu, Japan), and using a reverse phase column (Eurospher 100-5 C18 RP, Knauer, Germany, 250 × 4 mm i.d., 5 mm). The employed chromatographic conditions were described previously [24]. The mobile phase, a mixture of methanol/water (9:1, v/v), was applied at the following conditions: isocratic elution (15 min), and flow rate of 1 mL min^{-1} at 35 °C. Samples (5 µL) were injected to obtain chromatograms at 239 nm, and acetonitrile runs were used to clean the column between measurements. Calibration curves (R^2 = 0.999) were prepared from DXMT solutions of known concentration in methanol (0–45 mg mL^{-1}, for the drug incorporation experiments), and in water (0–55 µg mL^{-1}), for the released experiments.

2.13. Statistical analysis

The results are presented as mean ± standard error of the mean (SEM). Statistical analysis was performed with the Prism 5.03 Software for Windows (GraphPad Software, Inc, California, USA). The normality of the data was assessed with Shapiro–Wilk and Kolmogorov–Smirnov normality tests. Accordingly, data were analyzed with parametric and non-parametric tests, depending on the distribution of the data.

Drug release data was fitted by non-linear regression model using the JMP Pro 13 software (SAS, USA) to obtain the parameters of the diffusion and desorption models. The root-mean-square error (RMSE) was used to analyze the goodness of fit.

3. Results and discussion

3.1. Morphological and thermal characterization

Hydrophobic biodegradable polymers are used to obtain ophthalmic implants of several shapes including rods, plugs, pellets, disks and sheets [11,12]. The commonly used hydrophobic polymers for these purposes are poly(lactic acid) (PLA), poly(glycolic acid) (PGA), poly(lactic acid-co-glycolic acid) (PLGA) and poly(ε-caprolactone) (PCL) [11,12]. Cylindrical implants with dimensions of around 2 × 0.46 mm (length × diameter) were successfully obtained by SFM and HM processes. Important morphological properties of drug-free PCL-based implants were determined by helium pycnometry, nitrogen adsorption and mercury intrusion (Table 3).

Glycofurol (G, also known as tetraglycol, average M_n = 190.24 g mol^{-1}) is a safe and FDA-approved excipient in some pharmaceutical formulations (usually used as a hydrotrope). It is

Table 3
Morphological and thermal parameters of drug-free implants prepared by the SFM and HM processes.

Properties	PCL powder	Samples				
		PCL:DXMT:G (wt.%) (100:00:00)				(92:00:08)
		SFM (depressurization rate, MPa min^{-1})				HM
		1	2	3	2	
Nitrogen adsorption						
BET surface area ($m^2 \cdot g^{-1}$)	–	11.15 ± 0.28	15.95 ± 0.72	15.38 ± 0.52	11.46 ± 0.42	4.18 ± 0.16
BJH Average pore diameter (Å)	–	102.26	30.35	34.07	132.77	23.12
Mercury intrusion						
Average pore diameter (μm)	–	84.86	89.19	52.37	68.66	37.99
Porosity (%)	–	41.6	56.93	62.67	62.02	12.68
Bulk density ($g \cdot cm^{-3}$)	–	0.56	0.38	0.39	0.29	0.93
Helium pycnometry						
Real density ($g \cdot cm^{-3}$)	–	1.04 ± 0.03	0.99 ± 0.09	1.21 ± 0.07	1.06 ± 0.12	1.22 ± 0.05
Thermal properties						
T_m (°C)	60.99 ± 0.20	61.40 ± 0.27	61.66 ± 0.27	61.23 ± 0.31	61.15 ± 0.22	60.73 ± 0.18
ΔH_f (T_m)(J g^{-1})	105.70 ± 0.60	91.71 ± 0.08	90.64 ± 2.46	95.02 ± 0.58	92.08 ± 2.38	83.12 ± 1.31
X_c (%)	75.88 ± 0.43	65.84 ± 0.06	65.07 ± 1.77	68.21 ± 0.41	66.10 ± 1.71	59.67 ± 0.94

relatively non-toxic and non-irritant at the concentrations normally used for pharmaceutical applications, and presents a LD_{50} of 3.5 mL kg^{-1} (mouse, intravenous) [41]. In this work, glycofurol was used as a processing agent, namely as a pre-mixing solvent for the drug (DXMT), and as a DXMT-PCL compatibilizer.

As expected and as determined by helium pycnometry, HM and SFM-prepared materials presented similar real densities of 1.0–1.2 g cm^{-3}, which are clearly within the literature values range for pure PCL (0.99–1.22 g cm^{-3} [42,43]), and showing that the presence of glycofurol (similar density of 1.09 g cm^{-3}, as provided by the supplier) has a limited effect in real density.

The bulk densities of drug-free SFM-processed implants decreased with the depressurization rate from 0.56 g cm^{-3} (at 1 MPa min^{-1}) to 0.38–0.39 g cm^{-3} (at 2–3 MPa min^{-1}). Also, the addition of glycofurol led to a lower bulk density (0.29 g cm^{-3}). On the other hand, and as expected, HM-processed implants presented a bulk density of 0.93 g cm^{-3}, a value that is quite close to the real density, indicating low porosity.

Previous studies suggested that varying the final depressurization rate of the SFM-process could allow to control the porosity in PCL samples [19,44]. In this work, the porosity of SFM-processed glycofurol-free PCL implants increased with the depressurization rate (1–3 MPa min^{-1}) from 42 to 63 %, following the same trend reported elsewhere [21,45].

After the polymeric matrix swelling by CO_2 saturation, a fast decrease in pressure will induce a shift in equilibrium leading to an oversaturation of gaseous CO_2 inside the polymeric matrix. Different depressurization rates, at constant temperature, will lead to dissimilar phase separation pathways, and thus to distinct nucleation rates, number of nucleation sites and cavity/bubble sizes, all of which originating final different polymer morphologies, porosities, pore sizes/diameters, and pore interconnectivities/tortuosities). For faster depressurization rates, the energy barrier for nucleation usually decreases, leading to an increase of the nucleation rate and to the formation of a large number of smaller CO_2 bubbles, which will later originate a polymeric matrix presenting a large number of small size/diameter pores (mainly in the micro- and mesoporosity ranges), and high surface areas [46]. On the contrary, for slower depressurization rates, there is more time available for the diffusion of CO_2 into the forming bubbles, as well as to bubble coalescence and size growth. As a consequence, polymeric matrices will typically present less pores however of larger pore sizes/diameters and pore interconnectivities [42]. Therefore, as expected, average pore sizes, determined by mercury intrusion (in the 3–150 μm pore diameter measuring range), decreased from 85 to 89 to 52 μm as the depressurization rate was increased from 1 to 2 MPa min^{-1} to 3 MPa min^{-1}. For the same depressurization rate (2 MPa min^{-1}) and at the same pressure/temperature conditions, adding glycofurol slightly increased the porosity from 57 to 62 %, and decreased the average pore diameter from 89 to 69 μm (Table 3). These results suggest that, at this pore diameter range, glycofurol may also be playing a porogenic role. Unsurprisingly, HM-processed implants presented a much lower porosity (~13 %) and average pore diameter (~38 μm). Finally, at this pore diameter range, the average pore diameters obtained by mercury intrusion are in line with what can be observed by SEM (Fig. 1). These porosity/pore diameter differences can also be observed at the cross-sections of SFM- and HM-processed implants (Fig. 1). It should be noticed that SFM-processed samples are so porous that they deform during SEM sample preparation (Fig. 1).

Nitrogen adsorption/desorption isotherms (in the 3–150 nm pore diameter measuring range) show that SFM-processed glycofurol-free implants presented higher BET surface areas if compared to those processed by HM (~4.2 m^2 g^{-1}). In addition, the corresponding BET surface areas increased (from 11 to 15–16 m^2 g^{-1}) as the depressurization rates were increased from 1 to 2–3 MPa min^{-1}, thus showing the typical effect of the depressurization rate on the surface areas of CO_2-saturated thermoplastic polymers [46]. However, results also show that the addition of glycofurol decreased the BET surface area (from 16 to 11 m^2 g^{-1}) of the SFM-processed implants. Average pore sizes (BJH) obtained by this technique were within the microporous and mesoporous ranges for the SFM-processed implants, while lower values were obtained for the HM process (23 Å, in the microporous region). Again, the highest depressurization rates (2–3 MPa min^{-1}) decreased the average pore diameters of glycofurol-free implants (from 102 to 30–34 Å), as also reported by others [42,47].

Salerno et al. used ethyl lactate as an additive as a plasticizer and a blowing agent for the PCL foaming process, and in order to promote the formation of larger pores and lower pore density of PCL than by using pure CO_2 [48]. In the current work, the addition of glycofurol seems to have a similar effect on SFM-processed implants, originating larger pore diameters (from 30 to 133 Å) and smaller surface areas (as seen, from 16 to 11 m^2 g^{-1}) in the micro- and mesoporous ranges. On the contrary, and well beyond the lower limit of the macroporous range, the addition of glycofurol decreased pore diameters and increased porosity. Therefore, and in conclusion, the pore diameter analyses of SFM-

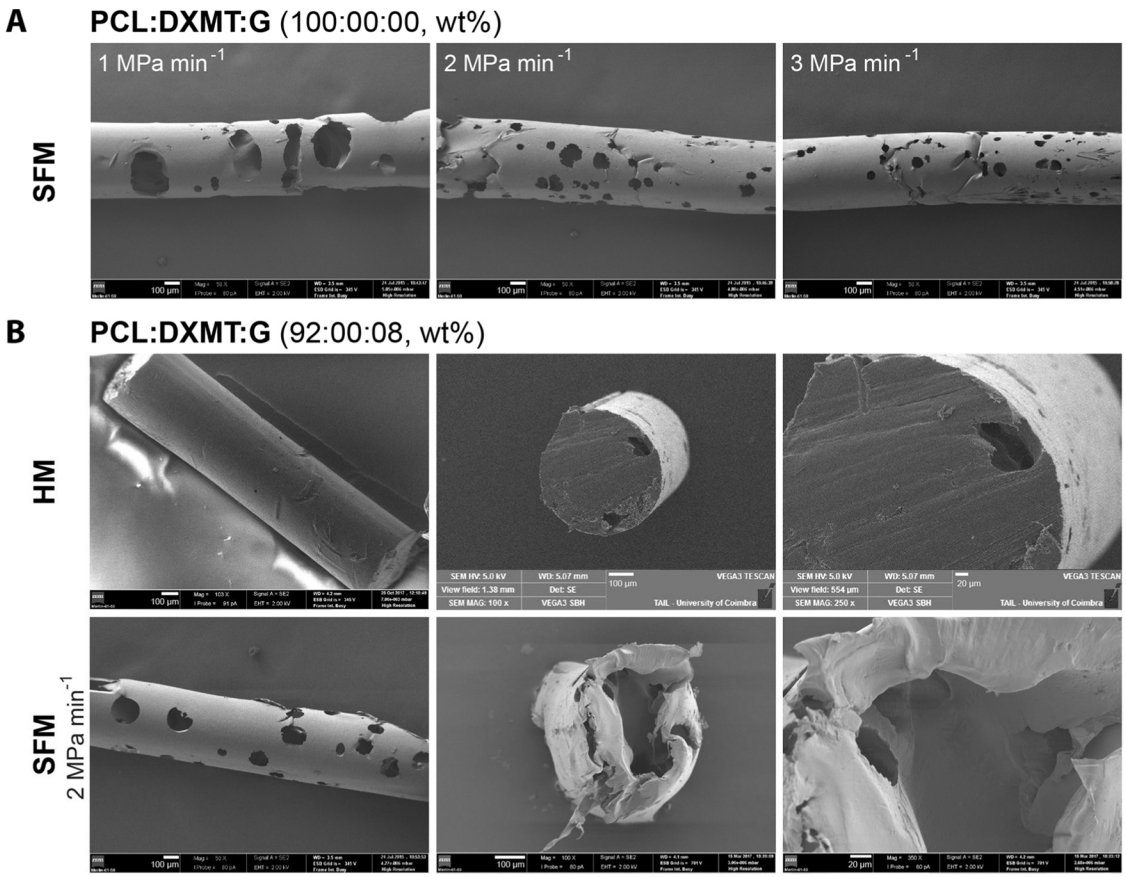

Fig. 1. SEM images of PCL (100:0:0, wt %) (A) or PCL:G (92:00:08, wt%) (B) implants processed by SFM (using different depressurization rates) and by HM. (B) Representative images of global views of the implants (left panel) and cross sections (middle and right panels).

processed implants, obtained both by nitrogen adsorption and by mercury intrusion, clearly shows the SFM process "tunability" in terms of the generation of all kinds of pore diameters in these implants, *i.e.*, from quite small to quite large pores, at the micro-, meso- and macroporous ranges, and simply by manipulating the depressurization rate or by adding small amounts of glycofurol. Micro- and mesopores (pore diameters below 50 nm), together with large surface areas (due to a large number of these small pores) are known to be important features for attaining faster degradation rates and/or for faster release of bioactive substances, while larger interconnected pores are known to be relevant for the transport of fluids and bioactive substances between implants and adjacent tissues [18,23,39,49]. Thus, the SFM methodology and the addition of small amounts of safe porogenic liquids clearly presents several additional advantages at the development of high porosity PCL-based implants and other materials for a wide range of pharmaceutical and biomedical applications.

Obtained MDSC thermograms presented one main melting point for all analysed samples (PCL powder and PCL-processed materials), which is typical of semi-crystalline thermoplastic polymers that went through thermal-based processing [17,19,27].

Typically, and during the SFM process, the sorption and the concentration of CO_2 within a semi-crystalline polymer increases as pressure increases, thus promoting a temporary plasticizing effect that enhances chain mobility and increases polymer free-volume. This process occurs firstly at the less-ordered (amorphous) regions of the polymer. As sorption continues, and as the chain mobility and free-volume keeps increasing, the ordered crystalline regions of the polymer will also be disarranged and the polymer will go easier through a phase of transition into a viscous molten state. Therefore, this transition will occur at a lower temperature than the polymer melting temperature at atmospheric pressure. The addition of a plasticizer can also help this process [42,48]. As explained before, after saturation and during the depressurization step, CO_2 will leave the molten polymer, forming gaseous cavities/bubbles by nucleation and growth, ending its role as a temporary plasticizer of the polymer. This will lead to the decrease of chain mobility and free-volume, causing the polymer to freeze. During this process, the polymer chains will rearrange again into amorphous (less ordered) and crystalline (more ordered) regions, whose relative extents may not be the same before processing. This means that the post-processing crystallinity degrees and the melting temperatures of semi-crystalline polymers may change due to the SFM process. For example, some studies indicated that SFM processing can significantly change (*i.e.*, increase or decrease) the pure PCL crystallinity degree, depending on the employed PCL properties (*e.g.*, original crystallinity, average molecular weight and molecular weight distribution), and on the employed operational conditions (*e.g.*, temperature, pressure, processing time) [21,42,50]. In this work, the obtained melting temperature of the PCL powder (60.99 ± 0.20 °C) was within the range specified by the supplier (56–64 °C), and both processing methods (SFM and HM) did not significantly affect the typical PCL melting temperature range. However, the enthalpies of fusion and, consequently, the crystallinity degrees decreased from 76 % (for PCL powder) to ~65–68 % (for SFM-processed implants, with or without the addition of glycofurol), and to 60 % (for HM-processed implants). The HM process led to a much more pronounced decrease in crystallinity than what was previously observed [51], however for slightly different HM operational conditions (1 h at 80 °C or at 150 °C).

3.2. Accelerated alkaline degradation tests

Previous studies confirmed that the *in vivo* PCL degradation follows a two-step hydrolytic-based process [16]. First, hydrolytic cleavage of

the ester linkage in the water insoluble polymer backbone occurs, producing lower molecular weight polymer segments (usually inferior to 5000). Then, these segments suffer further chain scission to produce even smaller fragments that could undergo biodegradation by phagocytosis [11,16,22].

PCL is known to follow a bulk erosion mechanism that is defined by a homogeneous reduction of its molecular weight [22,52,53]. The results are coherent with typical mass loss profiles that are obtained for those polymers undergoing bulk erosion [53,54]. In general, the aqueous medium has to diffuse first into PCL to promote random hydrolytic chain scission within the polymeric structure. Then, the newly formed degradation by-products (oligomers and monomers) may diffuse out to the release medium, or remain in the polymer bulk. If the latter happens, these by-products are also reported to prompt an internal autocatalytic degradation process due to the higher concentration of carboxylic acids (at the bulk), which may lead to some potentially harmful effects, namely in terms of the degradation of incorporated bioactive substances. On the other hand, their diffusion out to the surrounding medium may cause a sudden burst in the concentration of smaller oligomers, which may lead to some adverse tissue reactions, inducing inflammation (due to the locally decreased acidic pH conditions) [22].

PCL fully degrades *in vivo* after 2–4 years [16], which is a time frame that is not suitable for most of the *in vitro/in vivo* degradation tests required to employed to check the degradation of the produced intraocular implants. However, the accelerated hydrolytic degradation of polyesters can be attained by methods such as those using high temperature or, preferably, by those using strong acidic or alkaline media [22,53]. Nevertheless, high pH alkaline solutions were found to promote faster degradation rates than those attained in acidic conditions [55–57]. Thus, the degradation kinetics of drug-free 92:00:08 (wt.%) implants (processed both by SFM and by HM) were studied in a 5 M NaOH solution. These harsh and accelerated conditions allowed to determine and to compare the effects of the implant processing methodologies on their degradation rates (Fig. 2).

The erosion of SFM-processed implants was significant after 4 h, then followed a quasi-linear pattern with time. In contrast, the erosion of HM-processed implants was not significant until 32 h. Then, the observed mass loss also followed a clear linear pattern. These results confirm that, in these accelerated degradation conditions, the SFM process led to implants having properties that significantly help and increase the degradation rate of PCL, by attaining 50 % of mass loss within 31 h (compared to 59 h for the HM process), and 100 % (full degradation) around 69 h (compared to 81 h for the HM process). It should be mentioned that the obtained results presented higher variability near the end of the degradation test. This is due to a limitation in the methodology to accurately measure lower amounts of mass.

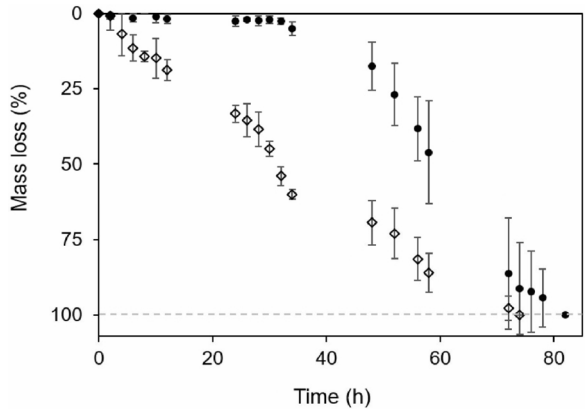

Fig. 2. Mass loss variation (%) *versus* time (h) for PCL:DXMT:G (92:00:08, wt%) implants prepared by: (●) HM (50 °C for 0.5 h, followed by 80 °C for 0.5 h); (◊) SFM (20 MPa, 45 °C, 2 h; depressurization rate of 2 MPa min^{-1}).

This means that the SFM process has the ability to originate implants presenting higher porosities and surface areas, which will be the main factors responsible for the faster degradation. These morphological properties will allow a faster water diffusion into PCL bulk, a larger number of hydrolyses sites (on surfaces), as well as a faster diffusion of the degradation products into the surrounding liquid Media. Properties such as PCL chain length, molecular weight distribution and, particularly, crystallinity, may have also an impact on the overall degradation process [22,53]. Higher values of crystallinity are known to increase the degradation time; however, slightly higher values of crystallinity were obtained for the SFM process (Table 3), which reinforces the importance of implant porosity and surface area explaining the different degradation rates obtained. Despite some expected differences, namely in terms of the periods that are indeed necessary to obtain 50 % and 100 % of degradation/erosion, the *in vivo* degradation of these implants are supposed to follow trends that are somehow similar to the behaviours that were observed at these accelerated conditions [22].

3.3. *In vitro evaluation of the effects of SFM-processed drug-free PCL-based implants*

From the characterization of the implants previously described, SFM drug-free glycofurol containing PCL-based (92:00:08, wt.%) implants were selected to proceed to biological assays. Primary retinal neural cell cultures were exposed to PCL-based implants for 6 consecutive days. The time necessary for the degradation of PCL-based materials is usually long, and the polymer degradation products can be a major factor influencing the tolerance of the developed implant [16]. Therefore, PCL-based implants were placed in culture medium for 3 weeks, which was then used to culture the cells for 6 days. The effect of the implant or the medium containing degradation products of PCL-based implants to the death of retinal neural cells was evaluated by TUNEL assay. Furthermore, the survival of retinal neurons was determined by counting the NeuN-immunoreactive cells (neuronal marker) (Fig. 3A).

The exposure of retinal cells to the implant or to the medium containing degradation products of PCL-based implants did not alter the number of $TUNEL^+$ cells (100 ± 3.3 % of the control and 105 ± 4.8 % of the control, respectively) when comparing with control conditions (Fig. 3B). Moreover, the number of $NeuN^+$ cells in culture was not significantly different in the three conditions (Fig. 3C). The degradation products of intraocular implants placed in the vitreous cavity would easily affect RGCs. Therefore, the toxicity of PCL-based implants to RGCs was also determined by exposing retinal organotypic cultures to PCL-based implants or by incubation with the medium previously in contact with the implant. The number of RGCs in cultured retinal explants was determined following immunolabeling for Brn3a (Fig. 3D), a marker of RGCs [58,59]. The presence of PCL-based implants for 24 h, 48 h or 72 h did not affect the number of RGCs in the retinal explants (115 ± 6.4 % of the control; 106 ± 4.2 % of the control; 103 ± 2.2 % of the control, respectively), indicating that PCL implants do not elicit RGC loss in organotypic cultures. Moreover, the incubation with medium containing degradation products of PCL-based implants did not significantly change the number of RGCs (95 ± 11.6 % of the control) (Fig. 3E).

The use of *in vitro* models, as a simplified system, presents several advantages to study the impact of PCL-based implants to retinal neurons. In fact, these retinal cell cultures are composed by the different cell types present in the retina as neurons and glial cells [60]. One of the limitations of retinal cell cultures is the loss of tissue architecture, which can be circumvented using retinal organotypic cultures. The vitreous body and neural retina are separated from each other by the inner limiting membrane (ILM), posing a barrier for drug delivery to the retina when an implant is placed intravitreally. An additional advantage of using *in vitro* models relates to the fact that is possible to evaluate the retinal cells tolerance to the PCL-based implant without

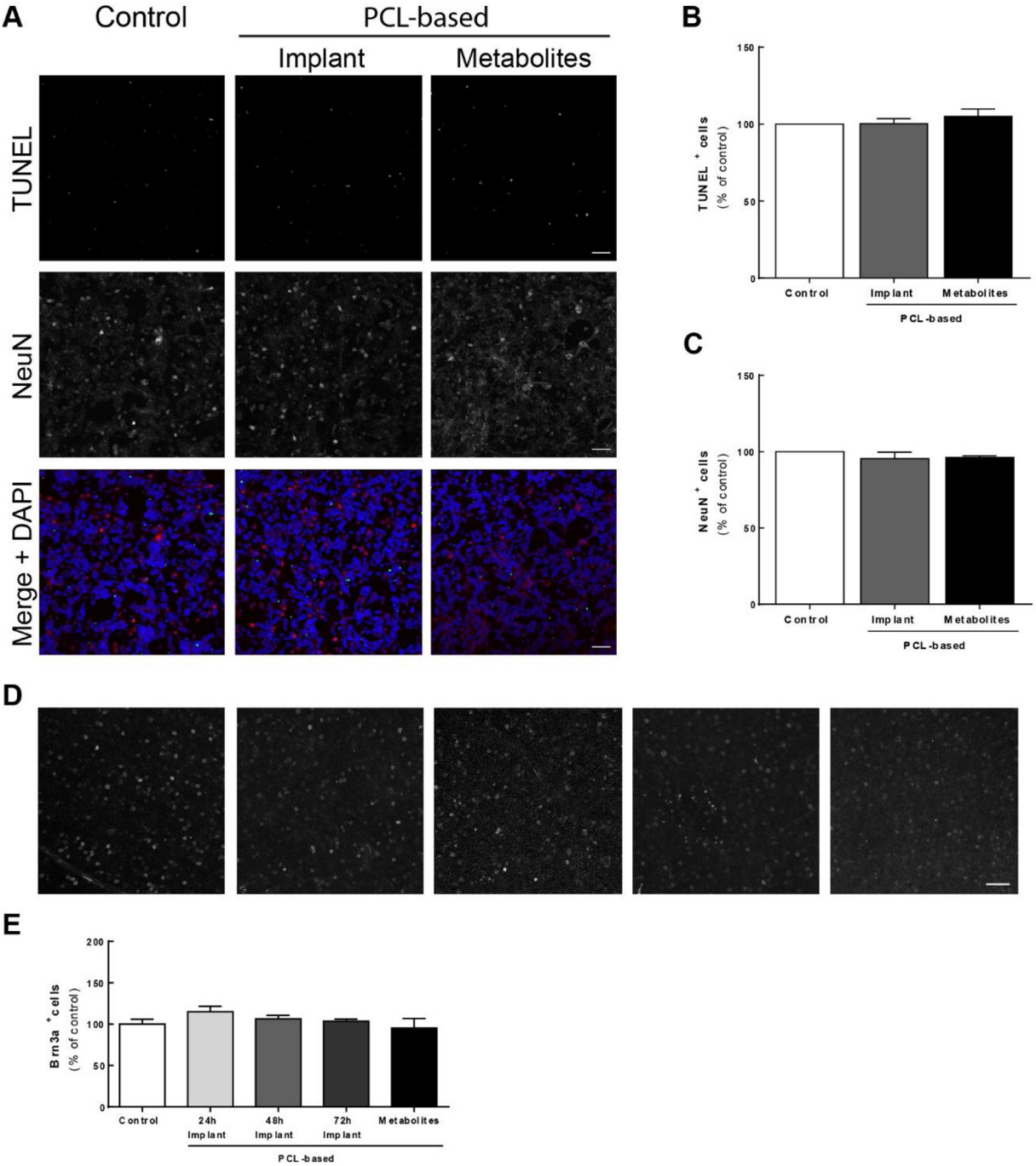

Fig. 3. The PCL-based implant (PCL:G (92:00:08, wt%)) or its degradation products did not induce cell death and neuronal loss in retinal primary neural cell cultures or RGC loss in retinal organotypic cultures. (A) Primary retinal neural cell cultures were incubated with PCL-based implant or with its metabolites for 6 consecutive days. Cell death was assessed by TUNEL assay and neurons were identified by immunocytochemistry with an anti-neuronal nuclear protein (NeuN). Nuclei were counterstained with DAPI (blue) and representative images are depicted, scale bar = 50 μm. (B) The number of TUNEL$^+$ cells per field was counted and the results are expressed as percentage of control from 3 to 6 independent experiments. (C) The number of NeuN-immunoreactive cells per field was counted and the results are expressed as percentage of control from 3 to 7 independent experiments. (D) Retinal organotypic cultures were incubated with PCL-based implants for 24 h, 48 h and 72 h or with its metabolites for 4 consecutive days. Retinal ganglion cells were immunostained for Brn3a and representative images are depicted, scale bar = 50 μm. (E) The number of Brn3a$^+$ cells were counted and the results are expressed as percentage of control from 3 to 4 independent experiments. (For interpretation of the references to colour in this figure legend, the reader is referred to the web version of this article.)

the presence of one of the barriers to drug delivery [61]. Therefore, by using these *in vitro* experimental models, we could conclude that SFM-PCL based implants could be tested in an animal model.

3.4. Evaluation of the effects of SFM-processed drug-free PCL-based implants on retinal structure and function

Since there was no toxicity associated to the PCL-based implants using *in vitro* models, PCL-based implants were introduced in the vitreous of Wistar rats for 4 and 8 weeks. Sham-operated animals were also assessed to verify whether the procedure caused alterations in the

Table 4
The PCL-based implant (PCL:G (92:00:08, wt%)) did not induce changes in animals IOP.

	4 weeks				8 weeks			
	Contra	Sham	Contra	Implant	Contra	Sham	Contra	Implant
Animal weight (g)	328 ± 20		322 ± 16		332 ± 29		348 ± 23	
IOP (mmHg)	13 ± 0.4	12 ± 0.3	14 ± 0.3	11 ± 0.2	12 ± 0.4	13 ± 0.4	12 ± 0.2	12 ± 0.3

The animals weight (g) and IOP (mmHg) were determined. IOP was measured bilaterally in animals after sham-operated or implantation procedure at 4 and 8 weeks. Contra, Contralateral eye; Sham, Sham-operated eye; Implant, Implanted eye.

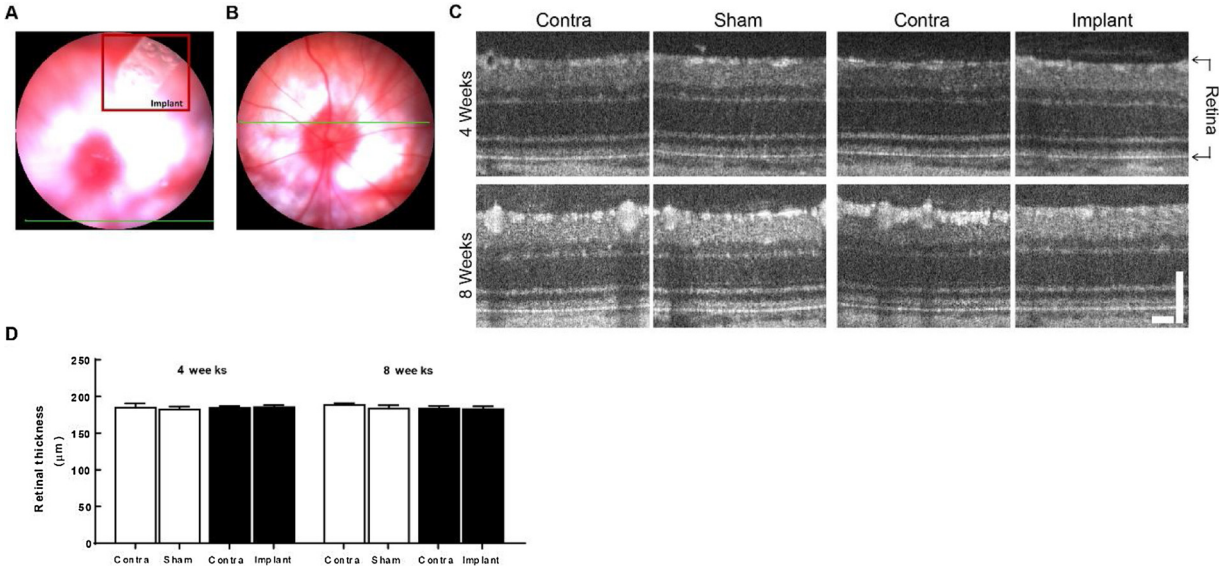

Fig. 4. The PCL-based implant (PCL:G (92:00:08, wt%)) did not change retinal structure evaluated *in vivo* by optical coherence tomography. PCL-based implant was introduced into the vitreous cavity using a 24-gauge catheter and 4 and 8 weeks after the animals were sacrificed. (A) Representative image of the vitreous cavity of the eye showing the presence of the implant. (B) Representative image of the eye fundus showing the OCT line scan (green line). (C) Representative images of OCT images showing the different retinal layers and the limits considered to measure total retinal thickness of the retinal layers, scale bars = 50 μm. (D) Total retinal thickness was measured and presented from 2 to 8 animals. Contra, Contralateral eye; Sham, Sham-operated eye; Implant, Implanted eye. (For interpretation of the references to colour in this figure legend, the reader is referred to the web version of this article.)

retina.

Throughout the experiment the weight and the IOP of the animals were monitored. No significant differences were detected in the weight of the animals (Table 4). IOP was regularly measured and no significant changes were found as well (Table 4).

The effect of PCL-based implants for 4 or 8 weeks on retinal structure and function was evaluated by optical coherence tomography (OCT) (Fig. 4) and electroretinography (ERG) (Table 5 and Fig. S1), respectively. These two methodologies have the advantage of being non-invasive and allow to follow the same animal throughout the course of the study.

By focusing the eye fundus image on the vitreous, it was possible to observe the PCL-based implant and confirm that the implant was not touching the retinal surface (Fig. 4A). OCT is a technique frequently used in the clinics that allows a real time imaging of the retina [62]. With this technique it is possible to clearly identify the different retinal layers: retinal nerve fiber layer (NFL), ganglion cell layer (GCL), inner plexiform layer (IPL), inner nuclear layer (INL), outer plexiform layer (OPL), outer nuclear layer (ONL), inner segments and the outer segments of photoreceptors (IS/OS) and outer limiting membrane (OLM) [63]. There are no alterations in retinal structure in sham-operated animals, as well as, in PCL implanted animals (Fig. 4C). The thickness of the total retinas was determined after image segmentation of the inner and outer limits (Fig. 4D). The surgical procedure necessary for the implantation of the PCL device (sham-operated animals) did not change retinal thickness (182 ± 4.3 μm and 184 ± 4.5 μm, at 4 and 8 weeks,

Table 5
The PCL-based implant (PCL:G (92:00:08, wt%)) did not change retinal activity evaluated by electroretinography.

		4 weeks				8 weeks			
		Contra	Sham	Contra	Implant	Contra	Sham	Contra	Implant
Scotopic a-wave	amplitude (μV)	190 ± 15	181 ± 14	258 ± 17	253 ± 9	172 ± 26	156 ± 1	177 ± 22	173 ± 16
	latency (ms)	10 ± 0.3	10 ± 0.2	10 ± 0.2	11 ± 0.2	10 ± 0.0	10 ± 0.0	10 ± 0.0	10 ± 0.0
Scotopic b-wave	amplitude (μV)	266 ± 19	259 ± 19	365 ± 21	360 ± 9	265 ± 5	251 ± 31	260 ± 29	265 ± 26
	latency (ms)	42 ± 4.8	43 ± 4.5	50 ± 0.4	51 ± 0.6	48 ± 1	48 ± 0.0	48 ± 0.9	49 ± 1.1

PCL-based implant was introduced into the vitreous cavity using a 24-gauge catheter and 4 and 8 weeks after the animals were sacrificed. The intensity-response functions relatively to the scotopic a-wave amplitude and latency and scotopic b-wave amplitude and latency were presented from 2 to 9 animals. Contra, Contralateral eye; Sham, Sham-operated eye; Implant, Implanted eye.

respectively) comparing with contralateral retinas. Also, the presence of the PCL implant did not change the thickness of the retinas (185 ± 2.9 μm; 183 ± 3.6 μm, at 4 and 8 weeks, respectively) when comparing with contralateral eye. These results suggest that both the procedure and the presence of the PCL-based implants did not elicit neither edema (that would cause an increase in retinal thickness) nor major cell loss (retinal thinning).

The retinal function was assessed by evaluating the electrical response of the retina to flash lights using ERG. The a- and b-wave amplitude and latency were extracted from scotopic ERG recordings at the maximum light intensity (9.49 cd-s m^{-2}) (Fig. S1). The a-wave amplitude (181 ± 13.8 μV and 156 ± 1.0 μV) and latency (10 ± 0.2 ms and 10 ± 0.0 ms) from sham-operated animals determined after 4 and 8 weeks, respectively, were not significantly different from contralateral retinas. Moreover, the procedure did not change b-wave amplitude and latency, at 4 and 8 weeks, respectively, comparing with contralateral eye. The presence of PCL-based implants during 4 and 8 weeks did not change a- and b-wave amplitude and latency, comparing with the contralateral retina (Table 5).

These results demonstrate that PCL implants can be easily inserted into the vitreous cavity by a minimally invasive procedure, not harmful to the retina. Moreover, the polymer demonstrates a strikingly good intraocular tolerance, which is in line with others demonstrating the biocompatibility of PCL implants [10,14,15,64–67]. Moreover, this study was able to go further by thoroughly characterize these PCL-based intraocular implants, using *in vivo* assessment of retinal structure and function.

3.5. Evaluation of the effects of SFM-processed drug-free PCL-based implants on retinal neurons

The effect of intraocular SFM-processed drug-free PCL-based implants on retinal neurons was assessed by immunolabelling the different cell types with specific antibodies (Fig. S2): cones with anti-arrestin (Fig. 5A); rods with anti-rhodopsin (Fig. 5B); horizontal cells with anti-calbindin (Fig. 5C); bipolar cells with anti-protein kinase C alpha (PKC-α) (Fig. 5D); amacrine cells with anti-choline acetyltransferase (ChAT) (Fig. 5E); and RGCs with anti-Brn3a (Fig. 6).

Both the procedure (sham-operated animals) and the presence of the PCL-based implant did not cause alterations in the morphology and density of the different cell types in the two periods analyzed (Fig. 5A–E). Moreover, both the distribution (Fig. 6A) and the total number (Fig. 6B) of $Brn3a^{+}$RGCs were assessed in retinal whole-mounts. Young and juvenile rats have a population of cells that project to the contralateral retina (retino-retinal projection) that constitutes 0.006 % to 0.03 % of the total RGC population [68]. The impact of PCL-based implants on the number of RGCs in the contralateral eye would allow to determine if this population of cells is affected. No alterations were detected in the distribution and total number of RGCs, when comparing naïve with contralateral retinas (naïve: 78,411 ± 1264 RGCsmm^{-2}) (Fig. S2B).

The surgical procedure did not change the number of RGCs (74,173 ± 2186 RGCsmm^{-2}; 76,186 ± 1983 RGCsmm^{-2}, at 4 and 8 weeks, respectively) comparing with contralateral retinas. Similarly, the presence of PCL-based implants in the vitreous for 4 and 8 weeks did not change the number of RGCs (71,354 ± 5595 RGCsmm^{-2}; 77,814 ± 2282 RGCsmm^{-2}, at 4 and 8 weeks, respectively) when compared with contralateral retinas (Fig. 6B).

These results demonstrated that the implants are not toxic to retinal neural cells using *in vitro* and animal models. Implants prepared from PCL have been studied in the field of ophthalmology [10,15]. The current work supports previous reports that indicate that PCL devices intravitreally implanted are well tolerated. In fact, the biocompatibility of PCL implants has been evaluated as subretinal [64,65], intracameral [14,66] and intravitreal [10,15,67] devices. Intravitreal PCL devices were shown to be well tolerated at short- and long-term, without fibrotic reaction, no sign of inflammation and minimal cell infiltration [10,15]. However, to the best of our knowledge this is the first study that evaluated the direct impact of PCL implants to retinal neurons.

3.6. Assessment of retinal glial cells reactivity

Retinal glial cells (microglia, astrocytes and Müller cells) [69] may become reactive as a consequence of reaction to foreign body biomaterials [70]. Chronic activation of these cells may be deleterious to the retina contributing to cell dysfunction and degeneration [31,34]. The impact of the surgical procedure and the effect of the presence of SFM-processed drug-free PCL-based implants on glial cells were assessed by immunohistochemistry in retinal vertical sections. Microglial cells were labelled with an antibody that recognizes ionized calcium-binding

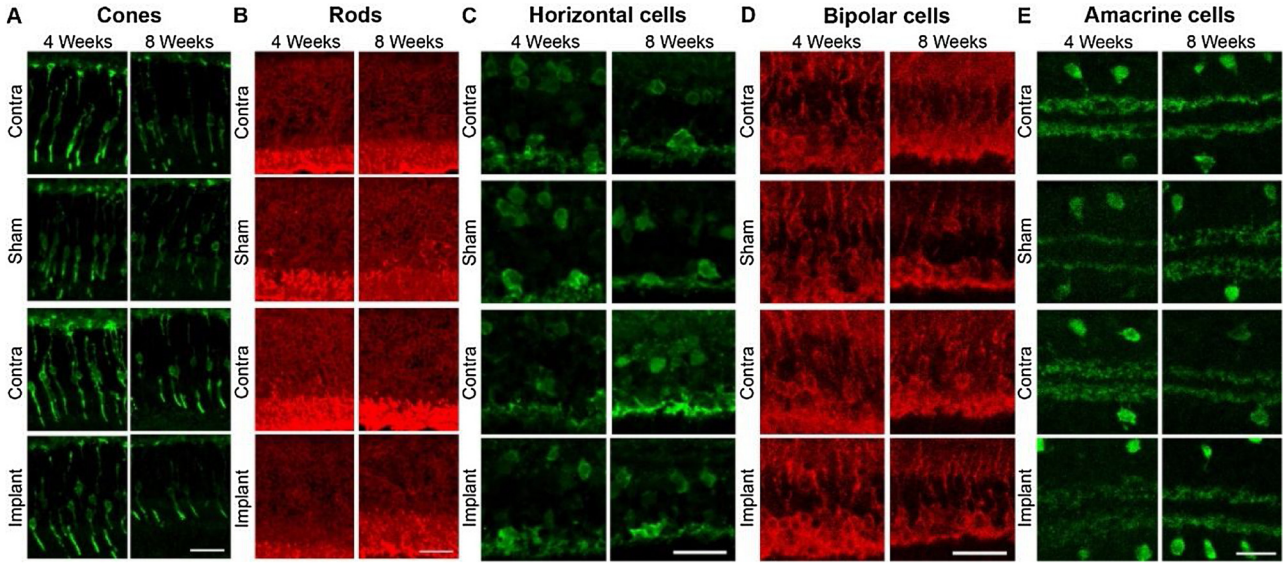

Fig. 5. The PCL-based implant (PCL:G (92:00:08, wt%)) did not induce alterations in retinal neurons. PCL-based implant was introduced into the vitreous cavity using a 24-gauge catheter and 4 and 8 weeks after the animals were sacrificed. Retinal cryosections were immunostainned for cones (arrestin) (A), rods (rohodopsin) (B), horizontal cells (calbindin) (C), bipolar cells (protein kinase C-α, PKC-α) (D) and amacrine cells (choline acetyltransferase, ChAT) (E). Representative images are depicted from 2 to 3 animals. Contra, Contralateral eye; Sham, Sham-operated eye; Implant, Implanted eye. Scale bar = 20 μm.

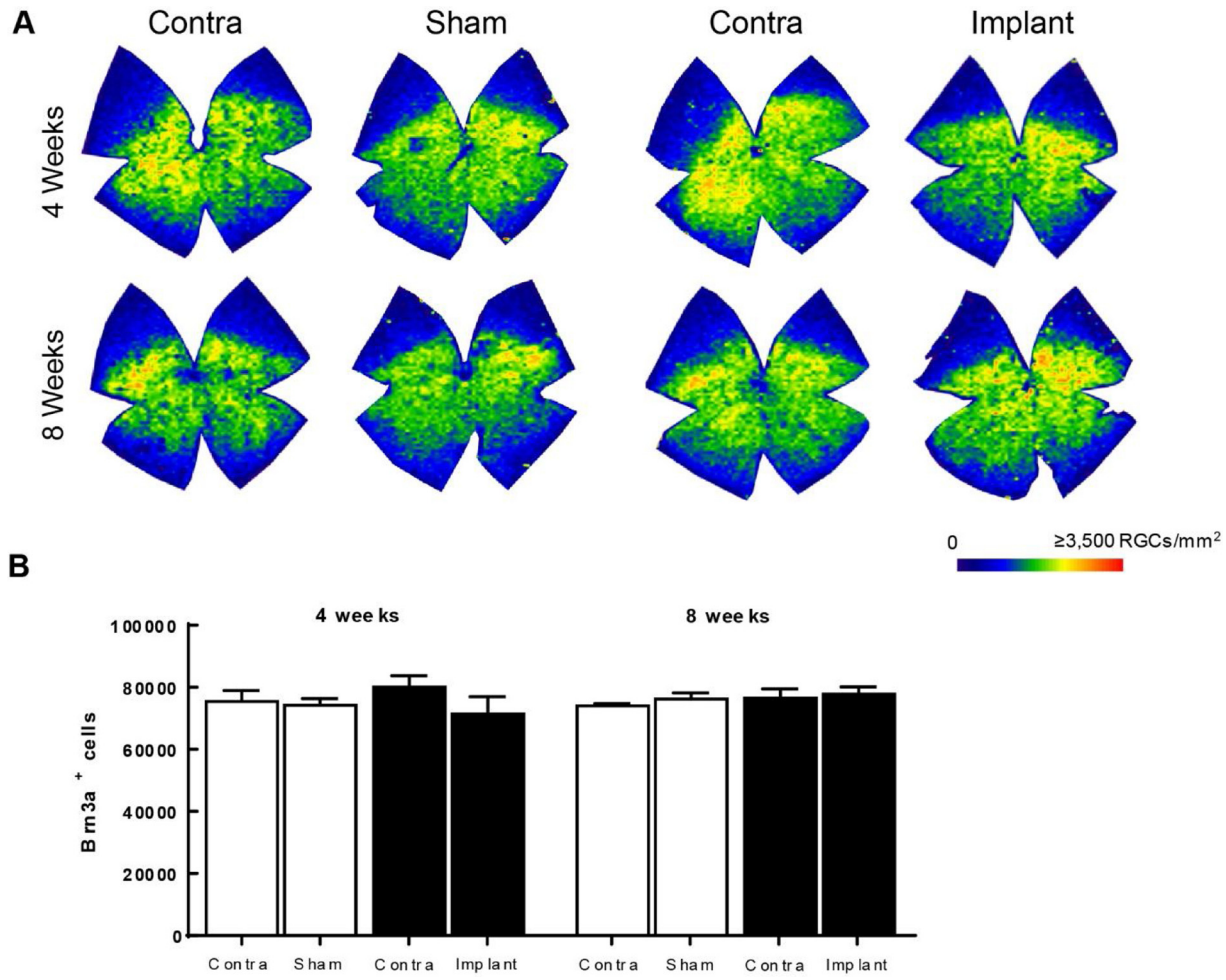

Fig. 6. The PCL-based implant (PCL:G (92:00:08, wt%)) did not change the number of RGCs. PCL-based implant was introduced into the vitreous cavity using a 24-gauge catheter and 4 and 8 weeks after the animals were sacrificed. (A) Retinal whole-mounts were immunostained for RGCs (Brn3a). Representative isodensity maps demonstrating the topological distribution of Brn3a$^+$RGCs are depicted, within a colour code of a 28-step colour scale range from 0 (dark blue) to 3500 or higher RGCs mm^{-2} (red). (B) The number of Brn3a$^+$RGCs was calculated from 3 to 7 animals. Contra, Contralateral eye; Sham, Sham-operated eye; Implant, Implanted eye. (For interpretation of the references to colour in this figure legend, the reader is referred to the web version of this article.)

adaptor molecule 1 (Iba1), astrocytes and Müller cell end feet were visualized by labelling glial fibrillary acidic protein (GFAP), and Müller cells with vimentin (Fig. 7).

Microglial cells have a key role in maintaining the homeostasis of the retinal environment and become reactive when detect alterations in the parenchyma [71], changing their morphology, a feature that is easily observed. No major changes were observed in the number, distribution and morphology of microglia for all conditions analyzed (Fig. 7A). Astrocytes have a preponderant role in the maintenance of physiological state of retina, namely neurotrophic support and the maintenance of the blood-retinal barrier [72]. Müller cells are the predominant glial cells in the retina, that traverse the entire retina, and modulate neuronal activity and keep homeostasis by regulating the extracellular levels of neurotransmitters [73]. GFAP is expressed by astrocytes [74], and it is also expressed at the end feet of retinal Müller cells in gliosis [75], thus suggesting that increased GFAP can be used as a marker of reactive glia [76].

In the contralateral retinas, the GFAP immunoreactivity was mainly observed in astrocytes, while in the retinas of the sham-operated animals or PCL implanted animals, GFAP was expressed in astrocytes but also found in the radial processes of Müller cells (Fig. 7B). Nevertheless, no major changes were observed for vimentin immunoreactivity, a protein mainly expressed by Müller cells (Fig. 7C). The increase in GFAP immunolabeling was further confirmed by western blot (Fig. S3). These results show that there is a foreign body reaction after PCL implantation, as well as due to surgical procedure, as assessed by the activation of Müller cells.

Müller cell reactive gliosis is a hallmark of retinal diseases [77,78], and this is characterized by a rapid increase in GFAP immunoreactivity that could be a sign of a disturbance in retinal homeostasis [79]. Increased GFAP in Müller cells, without alterations in microglia reactivity has been reported due to foreign body reaction [80,81]. In fact, 2 and 4 weeks after injection of poly(D,L-lactic-co-glycolic)acid microspheres, an increase in GFAP in Müller cells was observed, returning to normal levels after 12 and 24 months after injection [80]. Similar observations were reported after injection of PLGA microspheres that may induce retinal stress as evaluated by enhanced GFAP fluorescence [81]. In the retina, there is conflicting data whether gliosis is adverse or beneficial to the tissue. Müller cell gliosis could contribute to disease development and chronic gliosis might accelerate neurodegeneration, however, Müller cells under gliosis, in such conditions, can protect neurons by releasing neurotrophic factors [82]. The current work demonstrates that Müller cells become reactive following PCL implantation but also react to the surgical procedure, indicating that PCL implants per se do not elicit a change in these cells. This could be a response induced to protect neurons from a minimal disruption on retinal homeostasis due to surgical procedure.

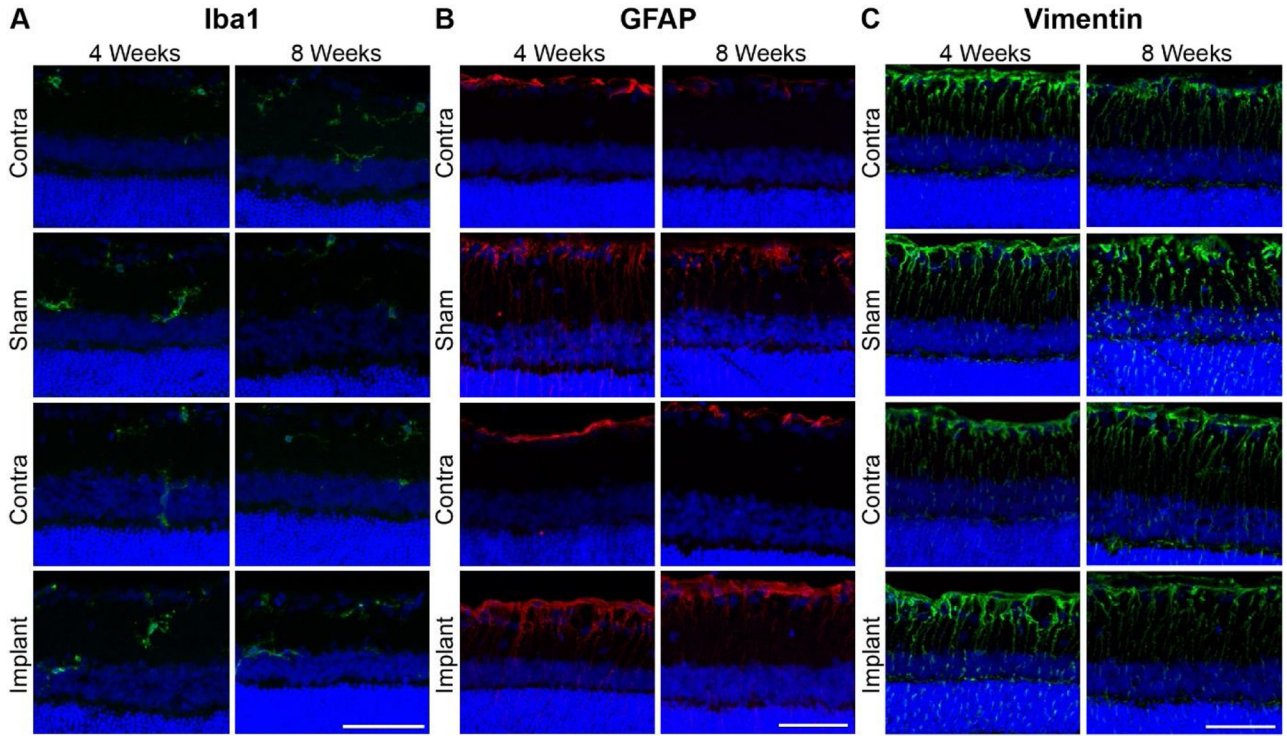

Fig. 7. The PCL-based implant (PCL:G (92:00:08, wt%)) may induce retinal stress evaluated by Müller cell gliosis. PCL-based implant was introduced into the vitreous cavity using a 24-gauge catheter and 4 and 8 weeks after the animals were sacrificed. Retinal cryosections were immunostainned for microglial cells (Iba1) (A), astrocytes (GFAP) (B) and Müller cells (vimentin) (C). Nuclei were stained with DAPI (blue). Representative images are depicted from 2 to 3 animals. Contra, Contralateral eye; Sham, Sham-operated eye; Implant, Implanted eye. Scale bar = 50 μm. (For interpretation of the references to colour in this figure legend, the reader is referred to the web version of this article.)

3.7. Assessment of the retinal inflammatory response

Taking into consideration that an adverse inflammatory reaction could negatively impact retinal function, inflammation was assessed in the presence of SFM-processed drug-free PCL-based implants, or of their degradation products, by quantifying the protein levels and the release of IL-1β and TNF, two pro-inflammatory cytokines that are known to mediate retinal damage [32]. The supernatants of primary retinal neural cell cultures (Fig. 8A, B), retinal organotypic cultures (Fig. 8C, D) and retinal protein extracts (Fig. 8E, F) were assayed by ELISA.

Regarding primary retinal neural cell cultures, in control conditions, the extracellular levels of IL-1β and TNF were 480.6 ± 360.5 pg mL^{-1} and 1.8 ± 1.1 pg mL^{-1}, respectively. The presence of the PCL-based implants, as well as the incubation with medium previously exposed to the implants did not change the levels of IL-1β (Fig. 8A) and TNF (Fig. 8B). In organotypic cultures, the levels of IL-1β and TNF in control conditions were 427.9 ± 99.6 pg mL^{-1} and 63.2 ± 16.4 pg mL^{-1}, respectively, and the presence of PCL-based implants or of their degradation products did not change the levels of IL-1β (Fig. 8C) and TNF (Fig. 8D).

Although there were no major effects of PCL-based implants or their degradation products when using cellular and tissue cultures, inflammation was also assessed in animals, since other signaling pathways could be involved. Retinal protein extracts from sham-operated and PCL-implanted animals (4 and 8 weeks post-surgery) were used to quantify IL-1β (Fig. 8E) and TNF (Fig. 8F). PCL-based implants did not significantly change the levels of IL-1β (18.4 ± 10.3 pg mL^{-1} of protein; 41.2 ± 22.4 pg mL^{-1} of protein) and TNF (4.8 ± 1.6 pg mL^{-1} of protein; 7.8 ± 2.2 pg mL^{-1} of protein) at 4 and 8 weeks, respectively, comparing with contralateral eyes. Moreover, the procedure used for the placement of the implants within the vitreous did not cause alterations in the IL-1β or TNF levels comparing with contralateral retinas.

Inflammation, secondary to implants presence, has been evaluated by the presence of cells or proteins in the vitreous or in the anterior chamber [10,15]. In our experiments, the PCL-based implants did not promote visible retinal infiltrations assessed by OCT analysis (Fig. 4). It is known that IL-1β and TNF are the main pro-inflammatory cytokines mediating retinal damage [32,83,84]. Therefore, the evaluation of the levels of these cytokines would provide a quantitative means of evaluating *in vitro* and in the animal model whether the exposure of retinal cells to PCL metabolites or implant would cause an inflammatory response. No alterations in the levels of IL-1β and TNF were detected, suggesting that PCL-based implants do not induce an inflammatory reaction in the retina.

3.8. Long-time exposure of retinal cells to a SFM-processed PCL-based implant

Since PCL has a slow degradation rate [16], we assessed the effects of the presence of a SFM-processed PCL-based implant after one year of implantation. Retinal structure was assessed by OCT and Müller cell gliosis was evaluated in retinal cryosections (Fig. 9).

Regarding retinal structure, even after a long period with a PCL-based device within the vitreous, no changes were found in the retinal structure (Fig. 9A). Also, the total retinal thickness was determined in the OCT images, and the presence of the PCL-based implant did not cause alterations in total retinal thickness (163 ± 4.7 μm) when comparing with contralateral retinas (168 ± 3.5 μm) (Fig. 9A).

Taking into consideration the observations consistent with Müller cell gliosis for the earliest time points, retinal cryosections were immunolabelled for GFAP. The GFAP immunoreactivity was mostly found in the nerve fiber layer, consistent with the staining of astrocytes (Fig. 9B), indicating that Müller cell gliosis observed in early time points after sham-operation and PCL-implantation is transient. Most likely, the initial reaction of Müller cells was necessary to maintain

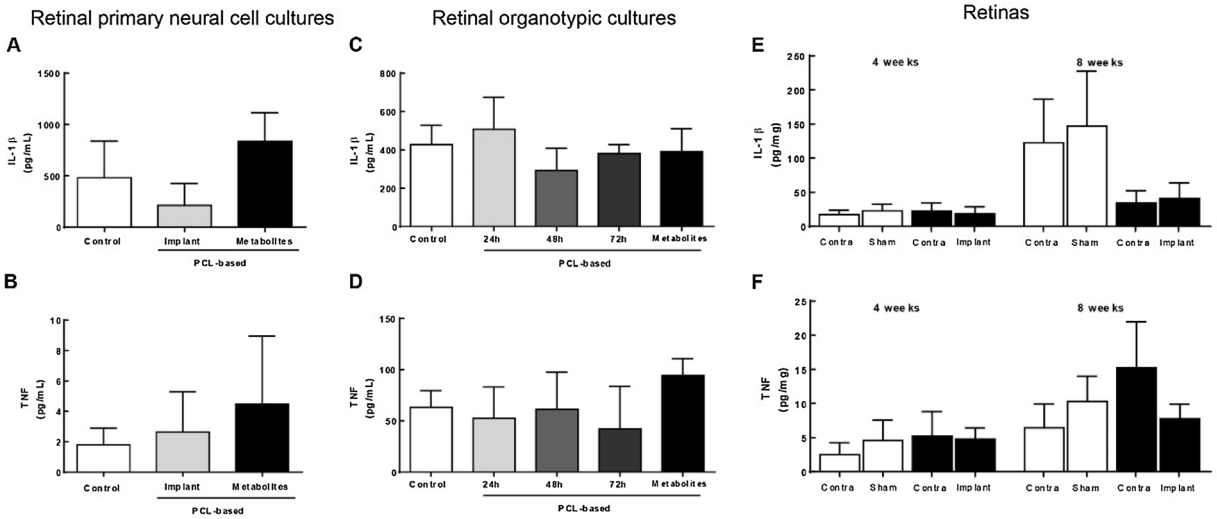

Fig. 8. The PCL-based implant (PCL:G (92:00:08, wt%)) or the degradation metabolites did not induce an inflammatory response *in vitro* or *in vivo*. Primary retinal neural cell cultures were incubated with PCL-based implants or with their metabolites for 6 consecutive days. Retinal organotypic cultures were incubated with PCL-based implants for 24 h, 48 h and 72 h or with their metabolites for 4 consecutive days. PCL-based implant was introduced into the vitreous cavity using a 24-gauge catheter and 4 and 8 weeks after the animals were sacrificed. IL-1β and TNF protein levels were assessed by ELISA in supernatant of retinal primary neural celld cultures (A, B) and of retinal organotypic cultures (C, D), and in retinal extracts (E, F). In culture supernatants the results are expressed in pg mL^{-1} of 2–4 independent experiments of primary cultures, and 2–12 animals independent experiments of organotypic cultures. For retinal extracts the results are expressed in pg mg^{-1} of protein of 7–11 animals. Contra, Contralateral eye; Sham, Sham-operated eye; Implant, Implanted eye.

retinal homeostasis after surgical procedure.

3.9. Drug incorporation yield and release

PCL-based implants prepared with glycofurol and loaded with DXMT (66:26:08 wt.%, PCL:DXMT:G) were prepared by both SFM and HM. DXMT is a corticosteroid used to treat eye inflammation and macular edema [85]. Its low solubility in water makes this drug a good candidate to be incorporated into the intraocular implant by the SFM process (aiming to increase its bioavailability). When using glycofurol, the drug incorporation yield achieved by the SFM process was around 99 % of the initially loaded DXMT (Table 1). However, glycofurol-free implants (74:26:00 wt.%, PCL:DXMT:G) showed a considerably lower drug incorporation yield (51 %). Liquid glycofurol has been used both as a co-solvent to dissolve drugs with low solubility in water [86] and was also proposed as a plasticizer for SFM-processed PCL-based materials [87]. In this work, and based on these incorporation yields, glycofurol also seems to be acting as a compatibilizer agent between DXMT and PCL.

The *in vitro* kinetics of DXMT release from SFM- and HM-processed implants (66:26:08 wt.%, PCL:DXMT:G) was performed at near infinite sink conditions, by keeping the concentration of DXMT 10 % below its saturation value in water (92–116 mg L^{-1} at 37 °C) [87,88]. The kinetics of DXMT release should present two distinct phases: (i) an initial burst, due to the release of DXMT deposited at pore surfaces of the implants; and (ii) a diffusive phase (after previous water sorption by the implants), and in which the drug diffuses out the implants. Any DXMT release favoured by bulk hydrolytic degradation of PCL-based implants,

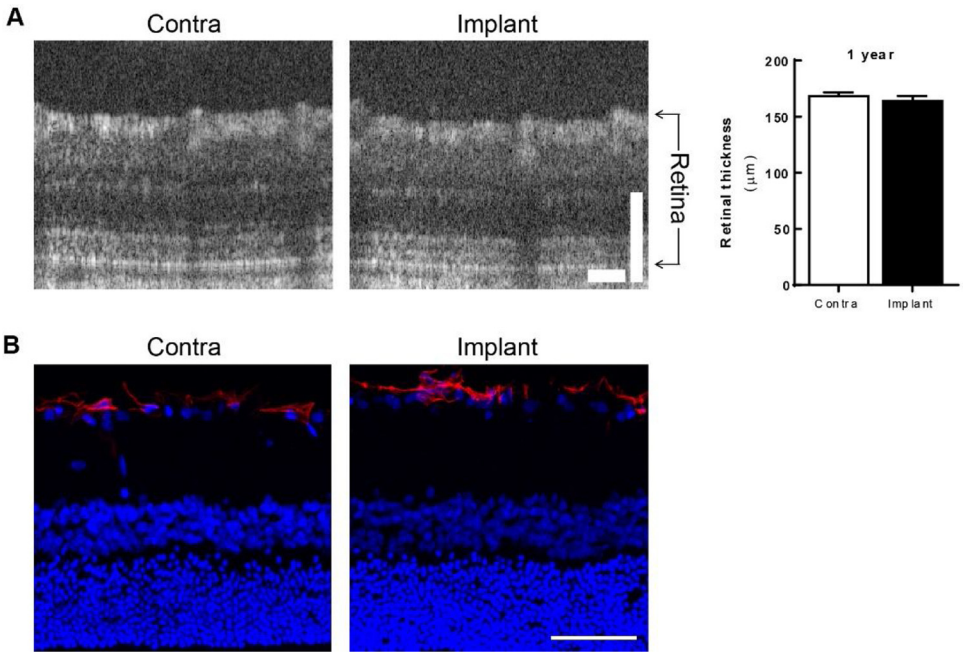

Fig. 9. Long-time exposure of retinal cells to the PCL-based implant PCL:G (92:00:08, wt%)) did not change retinal structure and did not induce Müller cell activation. PCL-based implant was introduced into the vitreous cavity using a 24-gauge catheter and 4 and 8 weeks after the animals were sacrificed. (A) Representative images of OCT images showing the different retinal layers, scale b*ARS* = 50 μm. Total retinal thickness was measured and presented from 1 animal. (B) Retinal cryosections were immunostainned for astrocytes (GFAP) and nuclei were stained with DAPI (blue). Representative images are depicted from 1 animal, scale bar = 50 μm. Contra, Contralateral eye; Implant, Implanted eye. (For interpretation of the references to colour in this figure legend, the reader is referred to the web version of this article.)

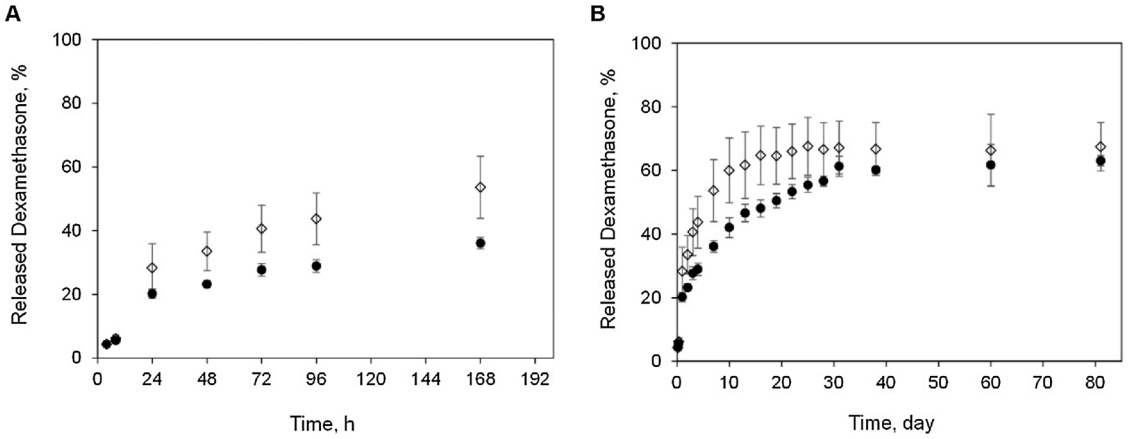

Fig. 10. Released DXMT (%) from implants (PCL:DXMT:G 66:26:08, wt.%) processed by SFM (◊) and by HM (●) considering hours (A) and days of drug release (B).

or to the final and abrupt release due to the collapse of the implants, cannot be clearly observed since the degradation of PCL is a very slow process in water.

The kinetics of DXMT release obtained for the SFM- and HM-processed implants was assessed (Fig. 10). For the initial release period, (Fig. 10A), SFM-processed implants release DXMT faster than implants processed by HM. This was certainly due to a more efficient mass transfer and diffusion processes and, as discussed in section 3.1, mostly due to their higher porosities (~57 %, in contrast with ~13 % for HM-processed implants) and surface areas (~16 $m^2 g^{-1}$, in contrast with ~4 $m^2 g^{-1}$ for HM-processed implants), as well as to the expected larger amounts of DXMT that were deposited on their pore surfaces (thus being more prone to be dissolved and released into the medium in a much faster way). In addition, the involved transfer and diffusion processes (of drug and/or release fluid) may also benefit from the larger pore diameters obtained for the SFM technique, both in the microporous range determined by nitrogen adsorption and well above the lower limit of the macroporous region determined by mercury intrusion. These observed distinct initial release profiles were later attenuated as the release period increased, and as the drug deposited on pore surfaces (or nearby) was released, leading to similar DXMT release profiles after 2–3 months, (Fig. 10B). The drug that was released, at these prolonged release periods, should essentially correspond to the DXMT impregnated (*i.e.*, molecularly dispersed) deeper into PCL struts. Moreover, and considering the initial DXMT loaded amounts (Table 1), it can be observed there was still around 35 % of non-released DXMT in the implants after 80 days of release, which suggests that these porous PCL implants can even be used for longer periods of time.

The obtained drug release data presented in Fig. 10 was correlated by two non-linear regression models: a diffusion-based model (Eq. (4)) and a desorption-based model (Eqs. (5) and (6)). Correlated parameters are indicated in Table 1. The goodness of fit for both models was confirmed by the relatively small RMSE values. Despite that the diffusion-based model was fitted only to release data points below 40 % of loaded drug, the correlated curves begin to deviate from the HM and SFM experimental points only after 10 and 13 days, respectively, which probably indicates an initial diffusion-controlled release process. HM-processed implants presented a smaller diffusion coefficient, thus confirming a more sustained kinetics of drug release, if compared with SFM-processed implants, and due to their lower porosities, surface areas and average pore diameters. However, this model should be applied carefully since it does not take into account any of the above referred morphological properties, all them known to strongly affect drug/fluid diffusion from/into solid polymeric matrices.

On the contrary, the desorption-based model can help us to infer about sample porosity effects on drug release kinetics. It can be observed that, and using this model, SFM-processed implants presented a higher porosity factor α (0.65) than that obtained for HM-processed implants (0.58), confirming that SFM-processed samples possess a higher fraction of DXMT deposited on pore surfaces, which is more readily available for release. On the other hand, HM-processed implants presented a higher specific process release time (7.5 days) than SFM-processed implants (3.8 days). This therefore confirms the more sustained DXMT release attained from HM-processed implants: steady state occurred after around 31 days, while it happened after 22 days for the SFM-processed implants.

The extended release periods attained for both HM and SFM-based implants were within the range reported for the commercially available Ozurdex implant (30 days) [89]. While Ozurdex releases 100 % of the loaded DXMT (700 μg) over 30 days, the HM- and SFM-processed implants release in this period around 61 % and 66 % of the initially loaded DXMT, respectively. Therefore, and as already discussed, these implants might still release the DMXT that was deeper impregnated in PCL for an additional period of time. In particular, and due to their enhanced porosity and surface area, the potential faster degradation of the SFM-processed implants and the additional DXMT release, can also be a further advantage which could potentially increase the commercial interest of these devices.

4. Conclusions

In order to circumvent the adverse effects of multiple intravitreal injections for drug delivery, several types of delivery systems have been proposed. In this work, a new porous PCL-based intraocular implant was successfully developed using a $scCO_2$ foaming/mixing (SFM) method. Glycofurol was used as a processing and compatibilizing agent between PCL and the model drug (DXMT), which led to much higher incorporation yields. The higher surface areas and porosities of SFM-processed implants led to faster alkaline hydrolytic degradation rates when compared to those implants processed by the conventional HM process. Moreover, these new porous PCL-based implants also presented a faster release rate of the test-drug (DXMT), namely for the initial releasing period, while HM-processed implants present a more sustained release behaviour. These results were confirmed by two release kinetics models (diffusion-based and desorption-based models)

The *in vitro* and *in vivo* biocompatibility of these new SFM-processed PCL-based implants was assessed. By *in vitro* studies, we demonstrated that the presence of PCL implants did not increase cell death, as well as, did not decrease the number of neurons in retinal primary neural cell cultures. Moreover, PCL implants did not reduce the number of Brn3a-immunoreactive RGCs in retinal organotypic cultures. By *in vivo* studies, the presence of PCL-based implants in the vitreous of Wistar rats did not change the values of IOP and did not cause changes in the retinal electrical activity nor in the structure. Moreover, PCL implants did not

induce alterations to retinal neurons, in particular did not change the number of RGCs. Nevertheless, both the procedure and the presence of PCL implants may induce Müller cells reactivity, without alterations in microglial cells and astrocytes, but the impact of this to retinal physiology is not known yet.

Taking into consideration the lack of retinal toxicity of the new SFM-processed PCL-based implants, we can envisage that these porous intraocular PCL implants can be used for long-term sustained intraocular drug delivery applications in several clinical conditions, thus avoiding the need of repeated intraocular injections. However, further comprehensive studies based on this promising preliminary assessment and proof-of-concept, should be performed in a near future, in order to enable the translation of these devices to the clinics.

Authors' contribution

HCS and MEMB have conceived and designed the porous implants concept, as well as their experimental production/processing, physicochemical characterization, and degradation/*in vitro* release experiments. PD performed the processing and characterization of degradation/*in vitro* drug release experiments. HCS, MEMB and PD analysed and interpreted the physicochemical characterization results, and the degradation/*in vitro* release experiments. RB and ARS conceived and designed the *in vitro* and *in vivo* experiments. RB, JMM, CGR, IDA performed the *in vitro* and *in vivo* experiments. RB, JMM, CGR, IDA and ARS analysed and interpreted the *in vitro* and *in vivo* results. MVS, MAB, AFA and ARS contributed with reagents, materials and analysis tools. RB wrote the first draft of the manuscript and all authors have read and approved the final version.

Funding

This work was financially supported by FCT, Portugal (Fellowships PD/BD/114115/2015, PD/BD/127821/2016, and SFRH/BPD/101048/2014, Grant PTDC/NEU-OSD/3123/2014 and Strategic Projects UID/NEU/04539/2013, PEst-C/EQB/UI0102/2013, PEst-C/EQB/UI0102/2018, and PEst-C/EQB/UI0102/2019), FEDER-COMPETE (FCOMP-01-0124-FEDER-028417 and POCI-01-0145-FEDER-007440) and Centro 2020 Regional Operational Programme (CENTRO-01-0145-FEDER-000008: Brain Health 2020).

Declaration of Competing Interest

None.

Appendix A. Supplementary data

Supplementary material related to this article can be found, in the online version, at doi:https://doi.org/10.1016/j.jconrel.2019.09.023.

References

[1] R.R.A. Bourne, S.R. Flaxman, T. Braithwaite, M.V. Cicinelli, A. Das, J.B. Jonas, et al., Magnitude, temporal trends, and projections of the global prevalence of blindness and distance and near vision impairment: a systematic review and meta-analysis, Lancet Glob. Health 5 (2017) e888–e897, https://doi.org/10.1016/S2214-109X(17)30293-0.

[2] V.K. Yellepeddi, S. Palakurthi, Recent advances in topical ocular drug delivery, J. Ocul. Pharmacol. Ther. 32 (2016) 67–82, https://doi.org/10.1089/jop.2015.0047.

[3] B. Sleath, A.L. Robin, D. Covert, J.E. Byrd, G. Tudor, B. Svarstad, Patient-reported behavior and problems in using glaucoma medications, Ophthalmology 113 (2006) 431–436, https://doi.org/10.1016/j.ophtha.2005.10.034.

[4] A.J. Claxton, J. Cramer, C. Pierce, A systematic review of the associations between dose regimens and medication compliance, Clin. Ther. 23 (2001) 1296–1310.

[5] G. Reardon, S. Kotak, G.F. Schwartz, Objective assessment of compliance and persistence among patients treated for glaucoma and ocular hypertension: a systematic review, Patient Prefer. Adher. 5 (2011) 441–463, https://doi.org/10.2147/PPA.S23780.

[6] B.L. Nordstrom, D.S. Friedman, E. Mozaffari, H.A. Quigley, A.M. Walker, Persistence and adherence with topical glaucoma therapy, Am. J. Ophthalmol. 140 (2005) 598–606, https://doi.org/10.1016/j.ajo.2005.04.051.

[7] Y.C. Kim, B. Chiang, X. Wu, M.R. Prausnitz, Ocular delivery of macromolecules, J. Control. Release 190 (2014) 172–181, https://doi.org/10.1016/j.jconrel.2014.06.043.

[8] K.M. Sampat, S.J. Garg, Complications of intravitreal injections, Curr. Opini. Ophthalmol. 21 (2010) 178–183, https://doi.org/10.1097/ICU.0b013e328338679a.

[9] T. Yasukawa, Y. Ogura, E. Sakurai, Y. Tabata, H. Kimura, Intraocular sustained drug delivery using implantable polymeric devices, Adv. Drug Deliv. Rev. 57 (2005) 2033–2046, https://doi.org/10.1016/j.addr.2005.09.005.

[10] A. Silva-Cunha, S.L. Fialho, M.C. Naud, F. Behar-Cohen, Poly-epsilon-caprolactone intravitreous devices: an in vivo study, Invest. Ophthalmol. Vis. Sci. 50 (2009) 2312–2318, https://doi.org/10.1167/iovs.08-2969.

[11] H. Kimura, Y. Ogura, Biodegradable polymers for ocular drug delivery, Ophthalmologica 215 (2001) 143–155, https://doi.org/10.1159/000050849.

[12] T. Yasukawa, Y. Tabata, H. Kimura, Y. Ogura, Recent advances in intraocular drug delivery systems, Recent Pat. Drug Deliv. Formul. 5 (2011) 1–10.

[13] J. Kim, M. Kudisch, N.R.K. da Silva, H. Asada, E. Aya-Shibuya, M.M. Bloomer, et al., Long-term intraocular pressure reduction with intracameral polycaprolactone glaucoma devices that deliver a novel anti-glaucoma agent, J. Control. Release 269 (2018) 45–51, https://doi.org/10.1016/j.jconrel.2017.11.008.

[14] J. Kim, M. Kudisch, S. Mudumba, H. Asada, E. Aya-Shibuya, R.B. Bhisitkul, et al., Biocompatibility and pharmacokinetic analysis of an intracameral polycaprolactone drug delivery implant for glaucoma, Invest. Ophthalmol. Vis. Sci. 57 (2016) 4341–4346, https://doi.org/10.1167/iovs.16-19585.

[15] S.L. Fialho, F. Behar-Cohen, A. Silva-Cunha, Dexamethasone-loaded poly(epsilon-caprolactone) intravitreal implants: a pilot study, Eur. J. Pharm. Biopharm. 68 (2008) 637–646, https://doi.org/10.1016/j.ejpb.2007.08.004.

[16] M.A. Woodruff, D.W. Hutmacher, The return of a forgotten polymer—polycaprolactone in the 21st century, Progr. Polym. Sci. 35 (2010) 1217–1256, https://doi.org/10.1016/j.progpolymsci.2010.04.002.

[17] M.B. de Matos, A.P. Piedade, C. Alvarez-Lorenzo, A. Concheiro, M.E. Braga, H.C. de Sousa, Dexamethasone-loaded poly(epsilon-caprolactone)/silica nanoparticles composites prepared by supercritical CO2 foaming/mixing and deposition, Int. J. Pharm. 456 (2013) 269–281, https://doi.org/10.1016/j.ijpharm.2013.08.042.

[18] M.B. de Matos, A.M. Puga, C. Alvarez-Lorenzo, A. Concheiro, M.E. Braga, H.C. de Sousa, Osteogenic poly(epsilon-caprolactone)/poloxamine homogeneous blends prepared by supercritical foaming, Int. J. Pharm. 479 (2015) 11–22, https://doi.org/10.1016/j.ijpharm.2014.12.041.

[19] A. Salerno, C. Domingo, Polycaprolactone foams prepared by supercritical CO_2 batch foaming of polymer/organic solvent solutions, J. Supercrit. Fluids 143 (2019) 146–156, https://doi.org/10.1016/j.supflu.2018.08.006.

[20] E. Di Maio, E. Kiran, Foaming of polymers with supercritical fluids and perspectives on the current knowledge gaps and challenges, J. Supercrit. Fluids 134 (2018) 157–166, https://doi.org/10.1016/j.supflu.2017.11.013.

[21] Y.-T. Shieh, H.-S. Yang, Morphological changes of polycaprolactone with high-pressure CO_2 treatment, J. Supercrit. Fluids 33 (2005) 183–192, https://doi.org/10.1016/j.supflu.2004.06.002.

[22] C.X. Lam, M.M. Savalani, S.H. Teoh, D.W. Hutmacher, Dynamics of in vitro polymer degradation of polycaprolactone-based scaffolds: accelerated versus simulated physiological conditions, Biomed. Mater. 3 (2008) 034108, https://doi.org/10.1088/1748-6041/3/3/034108.

[23] A. Vidaurre, J.M.M. Dueñas, J.M. Estellés, I.C. Cortázar, Influence of enzymatic degradation on physical properties of poly(ε-caprolactone) films and sponges, Macromol. Symp. 269 (2008) 38–46, https://doi.org/10.1002/masy.200850907.

[24] R.B. Chim, M.B.C. de Matos, M.E.M. Braga, A.M.A. Dias, H.C. de Sousa, Solubility of dexamethasone in supercritical carbon dioxide, J. Chem. Eng. Data 57 (2012) 3756–3760, https://doi.org/10.1021/je301065f.

[25] H. Kaji, T. Sugimoto, M. Kanatani, K. Nishiyama, K. Chihara, Dexamethasone stimulates osteoclast-like cell formation by directly acting on hemopoietic blast cells and enhances osteoclast-like cell formation stimulated by parathyroid hormone and prostaglandin E2, J. Bone Miner. Res. 12 (1997) 734–741, https://doi.org/10.1359/jbmr.1997.12.5.734.

[26] C.H. Kim, S.L. Cheng, G.S. Kim, Effects of dexamethasone on proliferation, activity, and cytokine secretion of normal human bone marrow stromal cells: possible mechanisms of glucocorticoid-induced bone loss, J. Endocrinol. 162 (1999) 371–379.

[27] M.V. Natu, M.H. Gil, H.C. de Sousa, Supercritical solvent impregnation of poly(ε-caprolactone)/poly(oxyethylene-*b*-oxypropylene-*b*-oxyethylene) and poly(ε-caprolactone)/poly(ethylene-vinyl acetate) blends for controlled release applications, J. Supercrit. Fluids 47 (2008) 93–102, https://doi.org/10.1016/j.supflu.2008.05.006.

[28] Y. Kong, J.N. Hay, The measurement of the crystallinity of polymers by DSC, Polymer 43 (2002) 3873–3878, https://doi.org/10.1016/s0032-3861(02)00235-5.

[29] D. Darwis, H. Mitomo, F. Yoshii, Degradability of radiation crosslinked PCL in the supercooled state under various environments, Poly. Degrad. Stab. 65 (1999) 279–285, https://doi.org/10.1016/s0141-3910(99)00017-8.

[30] A.R. Santiago, T.S. Pereira, M.J. Garrido, A.J. Cristovao, P.F. Santos, A.F. Ambrosio, High glucose and diabetes increase the release of [3H]-D-aspartate in retinal cell cultures and in rat retinas, Neurochem. Int. 48 (2006) 453–458, https://doi.org/10.1016/j.neuint.2005.10.013.

[31] M.H. Madeira, F. Elvas, R. Boia, F.Q. Goncalves, R.A. Cunha, A.F. Ambrosio, et al., Adenosine A2AR blockade prevents neuroinflammation-induced death of retinal ganglion cells caused by elevated pressure, J. Neuroinflammation 12 (2015) 115, https://doi.org/10.1186/s12974-015-0333-5.

[32] R. Boia, F. Elvas, M.H. Madeira, I.D. Aires, A.C. Rodrigues-Neves, P. Tralhao, et al., Treatment with A2A receptor antagonist KW6002 and caffeine intake regulate microglia reactivity and protect retina against transient ischemic damage, Cell

Death Dis. 8 (2017) e3065, https://doi.org/10.1038/cddis.2017.451.
[33] J. Martins, M. Castelo-Branco, A. Batista, B. Oliveiros, A.R. Santiago, J. Galvao, et al., Effects of 3,4-methylenedioxymethamphetamine administration on retinal physiology in the rat, PLoS One 6 (2011) e29583, https://doi.org/10.1371/journal.pone.0029583.
[34] M.H. Madeira, R. Boia, F. Elvas, T. Martins, R.A. Cunha, A.F. Ambrosio, et al., Selective A2A receptor antagonist prevents microglia-mediated neuroinflammation and protects retinal ganglion cells from high intraocular pressure-induced transient ischemic injury, Transl. Res. 169 (2016) 112–128, https://doi.org/10.1016/j.trsl.2015.11.005.
[35] M. Salinas-Navarro, S. Mayor-Torroglosa, M. Jimenez-Lopez, M. Aviles-Trigueros, T.M. Holmes, R.D. Lund, et al., A computerized analysis of the entire retinal ganglion cell population and its spatial distribution in adult rats, Vis. Res. 49 (2009) 115–126, https://doi.org/10.1016/j.visres.2008.09.029.
[36] F.I. Baptista, M.J. Pinto, F. Elvas, T. Martins, R.D. Almeida, A.F. Ambrosio, Diabetes induces changes in KIF1A, KIF5B and dynein distribution in the rat retina: implications for axonal transport, Exp. Eye Res. 127 (2014) 91–103, https://doi.org/10.1016/j.exer.2014.07.011.
[37] N.A. Peppas, L. Brannon-Peppas, Water diffusion and sorption in amorphous macromolecular systems and foods, J. Food Eng. 22 (1994) 189–210, https://doi.org/10.1016/0260-8774(94)90030-2.
[38] J. Siepmann, F. Lecomte, R. Bodmeier, Diffusion-controlled drug delivery systems: calculation of the required composition to achieve desired release profiles, J. Control. Release 60 (1999) 379–389, https://doi.org/10.1016/s0168-3659(99)00093-0.
[39] R. Srikar, A.L. Yarin, C.M. Megaridis, A.V. Bazilevsky, E. Kelley, Desorption-limited mechanism of release from polymer nanofibers, Langmuir 24 (2008) 965–974, https://doi.org/10.1021/la702449k.
[40] M.V. Natu, H.C. de Sousa, M.H. Gil, Effects of drug solubility, state and loading on controlled release in bicomponent electrospun fibers, Int. J. Pharm. 397 (2010) 50–58, https://doi.org/10.1016/j.ijpharm.2010.06.045.
[41] R.C. Rowe, P.J. Sheskey, Sn C. Owen, American Pharmacists Association, Raymond C. Rowe, Paul J. Sheskey, Siân C. Owen (Eds.), Handbook of Pharmaceutical Excipients, 5th ed., Pharmaceutical Press; American Pharmacists Association, London; Greyslake, IL Washington, DC, 2006.
[42] M.A. Fanovich, P. Jaeger, Sorption and diffusion of compressed carbon dioxide in polycaprolactone for the development of porous scaffolds, Mater. Sci. Eng. C 32 (2012) 961–968, https://doi.org/10.1016/j.msec.2012.02.021.
[43] A.A.J. Ketelaars, Y. Papantoniou, K. Nakayama, Analysis of the density and the enthalpy of poly(ε-caprolactone)-polycarbonate blends: amorphous phase compatibility and the effect of secondary crystallization, J. Appl. Polym. Sci. 66 (1997) 921–927, https://doi.org/10.1002/(sici)1097-4628(19971031)66:5<921::aid-app12>3.0.co;2-q.
[44] R.M.M. Churro, A.B.S. Rosa, M.B. de Matos, C. Alvarez-Lorenzo, A. Concheiro, M.E. Braga, et al., Safer and greener plasticizers, compatibilizers and foaming agents for the preparation of PCL/silica nanoparticles composite biomaterials, 2nd EuGSC – 2nd EuCheMS Congress on Green and Sustainable Chemistry, Lisbon, Portugal, 2015.
[45] R.M.M. Churro, Supercritical foaming/mixing on the Preparation of PCL/mesoporous Silica Based Composites for Hard Tissue Engineering Applications, Faculty of Sciences and Technology of University of Coimbra, 2015.
[46] L.J.M. Jacobs, M.F. Kemmere, J.T.F. Keurentjes, Sustainable polymer foaming using high pressure carbon dioxide: a review on fundamentals, processes and applications, Green Chem. 10 (2008) 731, https://doi.org/10.1039/b801895b.
[47] C.-X. Chen, H.-H. Peng, Y.-X. Guan, S.-J. Yao, Morphological study on the pore growth profile of poly(ε-caprolactone) bi-modal porous foams using a modified supercritical CO_2 foaming process, J. Supercrit. Fluids 143 (2019) 72–81, https://doi.org/10.1016/j.supflu.2018.07.029.
[48] A. Salerno, C.D. Pascual, A clean and sustainable route towards the design and fabrication of biodegradable foams by means of supercritical CO_2/ethyl lactate solid-state foaming, RSC Adv. 3 (2013) 17355, https://doi.org/10.1039/c3ra42345j.
[49] P. Shivanand, O.L. Sprockel, A controlled porosity drug delivery system, Int. J. Pharm. 167 (1998) 83–96, https://doi.org/10.1016/s0378-5173(98)00047-7.
[50] E. Kiran, K. Liu, K. Ramsdell, Morphological changes in poly(ε-caprolactone) in dense carbon dioxide, Polymer 49 (2008) 1853–1859, https://doi.org/10.1016/j.polymer.2008.02.017.
[51] A.M. Puga, A. Rey-Rico, B. Magarinos, C. Alvarez-Lorenzo, A. Concheiro, Hot melt poly-epsilon-caprolactone/poloxamine implantable matrices for sustained delivery of ciprofloxacin, Acta Biomater. 8 (2012) 1507–1518, https://doi.org/10.1016/j.actbio.2011.12.020.
[52] F. von Burkersroda, L. Schedl, A. Gopferich, Why degradable polymers undergo surface erosion or bulk erosion, Biomaterials 23 (2002) 4221–4231, https://doi.org/10.1016/S0142-9612(02)00170-9.
[53] B. Laycock, M. Nikolić, J.M. Colwell, E. Gauthier, P. Halley, S. Bottle, et al., Lifetime prediction of biodegradable polymers, Prog. Polym. Sci. 71 (2017) 144–189, https://doi.org/10.1016/j.progpolymsci.2017.02.004.
[54] E. Bat, Z. Zhang, J. Feijen, D.W. Grijpma, A.A. Poot, Biodegradable elastomers for biomedical applications and regenerative medicine, Regener. Med. 9 (2014) 385–398, https://doi.org/10.2217/rme.14.4.
[55] J. Rydz, W. Sikorska, M. Kyulavska, D. Christova, Polyester-based (bio)degradable polymers as environmentally friendly materials for sustainable development, Int. J. Mol. Sci. 16 (2014) 564–596, https://doi.org/10.3390/ijms16010564.
[56] J.H. Jung, M. Ree, H. Kim, Acid- and base-catalyzed hydrolyses of aliphatic polycarbonates and polyesters, Catal. Today 115 (2006) 283–287, https://doi.org/10.1016/j.cattod.2006.02.060.
[57] Aurelio Ramírez Hernández, Oscar Crisanto Contreras, Jorge Conde Acevedo, Leticia Guadalupe Navarro Moreno, Poly(ε-caprolactone) degradation under acidic and alkaline conditions, Am. J. Polym. Sci. 3 (2013) 70–75, https://doi.org/10.5923/j.ajps.20130304.02.
[58] F.M. Nadal-Nicolas, M. Jimenez-Lopez, P. Sobrado-Calvo, L. Nieto-Lopez, I. Canovas-Martinez, M. Salinas-Navarro, et al., Brn3a as a marker of retinal ganglion cells: qualitative and quantitative time course studies in naive and optic nerve-injured retinas, Invest. Ophthalmol. Vis. Sci. 50 (2009) 3860–3868, https://doi.org/10.1167/iovs.08-3267.
[59] F.M. Nadal-Nicolas, M. Jimenez-Lopez, M. Salinas-Navarro, P. Sobrado-Calvo, J.J. Alburquerque-Bejar, M. Vidal-Sanz, et al., Whole number, distribution and co-expression of brn3 transcription factors in retinal ganglion cells of adult albino and pigmented rats, PLoS One 7 (2012) e49830, https://doi.org/10.1371/journal.pone.0049830.
[60] A. Santos-Carvalho, C.A. Aveleira, F. Elvas, A.F. Ambrosio, C. Cavadas, Neuropeptide Y receptors Y1 and Y2 are present in neurons and glial cells in rat retinal cells in culture, Invest. Ophthalmol. Vis. Sci. 54 (2013) 429–443, https://doi.org/10.1167/iovs.12-10776.
[61] E.M. del Amo, A.-K. Rimpelä, E. Heikkinen, O.K. Kari, E. Ramsay, T. Lajunen, et al., Pharmacokinetic aspects of retinal drug delivery, Prog. Retin. Eye Res. 57 (2017) 134–185, https://doi.org/10.1016/j.preteyeres.2016.12.001.
[62] J.G. Fujimoto, Optical coherence tomography for ultrahigh resolution in vivo imaging, Nat. Biotechnol. 21 (2003) 1361–1367, https://doi.org/10.1038/nbt892.
[63] K. Adachi, S. Takahashi, K. Yamauchi, N. Mounai, R. Tanabu, M. Nakazawa, Optical coherence tomography of retinal degeneration in Royal College of Surgeons rats and its correlation with morphology and electroretinography, PLoS One 11 (2016) e0162835, https://doi.org/10.1371/journal.pone.0162835.
[64] S. Shahmoradi, F. Yazdian, F. Tabandeh, Z.S. Soheili, A.S. Hatamian Zarami, M. Navaei-Nigjeh, Controlled surface morphology and hydrophilicity of polycaprolactone toward human retinal pigment epithelium cells, Mater. Sci. Eng. C 73 (2017) 300–309, https://doi.org/10.1016/j.msec.2016.11.076.
[65] N.R. Beeley, J.V. Rossi, P.A. Mello-Filho, M.I. Mahmoud, G.Y. Fujii, E. de Juan Jr.et al., Fabrication, implantation, elution, and retrieval of a steroid-loaded polycaprolactone subretinal implant, J. Biomed. Mater. Res. A 73 (2005) 437–444, https://doi.org/10.1002/jbm.a.30294.
[66] D.A. Bernards, R.B. Bhisitkul, P. Wynn, M.R. Steedman, O.T. Lee, F. Wong, et al., Ocular biocompatibility and structural integrity of micro- and nanostructured poly (caprolactone) films, J. Ocul. Pharmacol. Ther. 29 (2013) 249–257, https://doi.org/10.1089/jop.2012.0152.
[67] K.D. Lance, S.D. Good, T.S. Mendes, M. Ishikiriyama, P. Chew, L.S. Estes, et al., In vitro and in vivo sustained zero-order delivery of rapamycin (Sirolimus) from a biodegradable intraocular device, Invest. Ophthalmol. Vis. Sci. 56 (2015) 7331–7337, https://doi.org/10.1167/iovs.15-17757.
[68] F.M. Nadal-Nicolas, F.J. Valiente-Soriano, M. Salinas-Navarro, M. Jimenez-Lopez, M. Vidal-Sanz, M. Agudo-Barriuso, Retino-retinal projection in juvenile and young adult rats and mice, Exp. Eye Res. 134 (2015) 47–52, https://doi.org/10.1016/j.exer.2015.03.015.
[69] P.A. Tresco, B.D. Winslow, The challenge of integrating devices into the central nervous system, Crit. Rev. Biomed. Eng. 39 (2011) 29–44, https://doi.org/10.1615/CritRevBiomedEng.v39.i1.30.
[70] J.M. Anderson, A. Rodriguez, D.T. Chang, Foreign body reaction to biomaterials, Semin. Immunol. 20 (2008) 86–100, https://doi.org/10.1016/j.smim.2007.11.004.
[71] S.A. Wolf, H.W. Boddeke, H. Kettenmann, Microglia in physiology and disease, Annu. Rev. Physiol. 79 (2017) 619–643, https://doi.org/10.1146/annurev-physiol-022516-034406.
[72] E. Vecino, F.D. Rodriguez, N. Ruzafa, X. Pereiro, S.C. Sharma, Glia-neuron interactions in the mammalian retina, Prog. Retin. Eye Res. 51 (2016) 1–40, https://doi.org/10.1016/j.preteyeres.2015.06.003.
[73] E. Newman, A. Reichenbach, The Muller cell: a functional element of the retina, Trends Neurosci. 19 (1996) 307–312, https://doi.org/10.1016/0166-2236(96)10040-0.
[74] M.V. Sofroniew, H.V. Vinters, Astrocytes: biology and pathology, Acta Neuropathol. 119 (2010) 7–35, https://doi.org/10.1007/s00401-009-0619-8.
[75] C. Lupien, M. Brenner, S.L. Guerin, C. Salesse, Expression of glial fibrillary acidic protein in primary cultures of human muller cells, Exp. Eye Res. 79 (2004) 423–429, https://doi.org/10.1016/j.exer.2004.05.008.
[76] G.P. Lewis, S.K. Fisher, Up-regulation of glial fibrillary acidic protein in response to retinal injury: its potential role in glial remodeling and a comparison to vimentin expression, Int. Rev. Cytol. 230 (2003) 263–290, https://doi.org/10.1016/s0074-7696(03)30005-1.
[77] M. Mizutani, C. Gerhardinger, M. Lorenzi, Muller cell changes in human diabetic retinopathy, Diabetes 47 (1998) 445–449, https://doi.org/10.2337/diabetes.47.3.445.
[78] L. Wang, G.A. Cioffi, G. Cull, J. Dong, B. Fortune, Immunohistologic evidence for retinal glial cell changes in human glaucoma, Invest. Ophthalmol. Vis. Sci. 43 (2002) 1088–1094.
[79] T.D. Kimble, M.E. Fitzgerald, A. Reiner, Sustained upregulation of glial fibrillary acidic protein in Muller cells in pigeon retina following disruption of the parasympathetic control of choroidal blood flow, Exp. Eye Res. 83 (2006) 1017–1030, https://doi.org/10.1016/j.exer.2006.05.006.
[80] G.G. Giordano, P. Chevez-Barrios, M.F. Refojo, C.A. Garcia, Biodegradation and tissue reaction to intravitreous biodegradable poly(D,L-lactic-co-glycolic)acid microspheres, Curr. Eye Res. 14 (1995) 761–768, https://doi.org/10.3109/02713689508995797.
[81] M. Zhao, E. Rodriguez-Villagra, L. Kowalczuk, M. Le Normand, M. Berdugo, R. Levy-Boukris, et al., Tolerance of high and low amounts of PLGA microspheres

loaded with mineralocorticoid receptor antagonist in retinal target site, J. Control. Release 266 (2017) 187–197, https://doi.org/10.1016/j.jconrel.2017.09.029.
[82] A. Bringmann, T. Pannicke, J. Grosche, M. Francke, P. Wiedemann, S.N. Skatchkov, et al., Muller cells in the healthy and diseased retina, Prog. Retin. Eye Res. 25 (2006) 397–424, https://doi.org/10.1016/j.preteyeres.2006.05.003.
[83] S. Berger, S.I. Savitz, S. Nijhawan, M. Singh, J. David, P.S. Rosenbaum, et al., Deleterious role of TNF-alpha in retinal ischemia-reperfusion injury, Invest. Ophthalmol. Vis. Sci. 49 (2008) 3605–3610, https://doi.org/10.1167/iovs.07-0817.
[84] S. Yoneda, H. Tanihara, N. Kido, Y. Honda, W. Goto, H. Hara, et al., Interleukin-1beta mediates ischemic injury in the rat retina, Exp. Eye Res. 73 (2001) 661–667, https://doi.org/10.1006/exer.2001.1072.
[85] P.U. Dugel, F. Bandello, A. Loewenstein, Dexamethasone intravitreal implant in the treatment of diabetic macular edema, Clin. Ophthalmol. 9 (2015) 1321–1335, https://doi.org/10.2147/OPTH.S79948.
[86] N.S. Barakat, Evaluation of glycofurol-based gel as a new vehicle for topical application of naproxen, AAPS PharmSciTech 11 (2010) 1138–1146, https://doi.org/10.1208/s12249-010-9485-x.
[87] R.M.M. Churro, A.B.S. Rosa, M.E. Braga, H.C. Sousa, Supercritical CO_2 foaming/mixing for the preparation of plasticized porous PCL/SBA-15 composite biomaterials, Prosciba 2016 – IV Iberoamerican Conference on Supercritical Fluids, Chile, 2016.
[88] S. Yalkowsky, Y. He, P. Jain, Handbook of Aqueous Solubility Data, CRC Press, 2010.
[89] B.G. Amsden, D. Marecak, Long-term sustained release from a biodegradable photo-cross-linked network for intraocular corticosteroid delivery, Mol. Pharm. 13 (2016) 3004–3012, https://doi.org/10.1021/acs.molpharmaceut.6b00358.